Climate Dynamics (2026) 64:322
https://doi.org/10.1007/s00382-026-08278-x

North Atlantic circulation and climate variability during the last glacial maximum and the last interglacial: insights from CMIP6/PMIP4 climate models

Deepak Kumar Chinnaswamy[1] · Sebastian Wagner[2] · Michael Hein[3,4,5] · Marie-Luise Kapsch[6] · Antje Schwalb[1]

Received: 2 March 2026 / Accepted: 16 June 2026

Abstract
The Last Glacial Maximum (LGM) and Last Interglacial (LIG) provide insights into the response of the North Atlantic–European climate variability to strongly contrasting boundary conditions. Using six CMIP6/PMIP4 models, we compare temperature–precipitation patterns, atmospheric circulation, and variability, with emphasis on the North Atlantic Oscillation (NAO). Across climate states, the leading modes of wintertime sea-level pressure variability remain recognisable, indicating a robust dynamical structure. However, their amplitude, explained variance, and spatial positioning exhibit state dependence. During the LGM, extensive ice sheets were associated with a stronger and more spatially confined NAO dipole, southward-displaced pressure centres, and reorganised circulation patterns, reinforcing colder and drier European conditions with enhanced seasonality. The LIG exhibits a weaker NAO expression with westward-shifted pressure centres, a more zonal circulation, northward-shifted warm sea surface temperatures, and enhanced seasonality. NAO-related interannual atmosphere–ocean coupling persists across climate states, with limitations in capturing low-frequency variability within the available simulation lengths. Summer variability is substantially weaker and more heterogeneous across all periods, with the NAO losing dominance often to the East Atlantic pattern during the LGM. Inter-model differences increase considerably under LGM and LIG conditions compared to the pre-industrial period (PI), underscoring the importance of multi-model approaches and an improved representation of key processes when investigating climate variability in extreme climate states.

Keywords LGM · LIG · Interannual variability · NAO · PMIP4 · North Atlantic teleconnections · SSTs

1 Introduction

The variability of the North Atlantic atmospheric circulation plays a central role in shaping European climate, particularly on sub-decadal timescales (Årthun et al. 2018; Cariou et al. 2025), with oceanic influence becoming dominant over longer periods (Årthun et al. 2018; Sutton and Hodson 2005). A large fraction of this variability is commonly described by the North Atlantic Oscillation (NAO) (Hurrell 1995; Hurrell and Deser 2009), which represents the leading mode of atmospheric circulation over the North Atlantic–European sector and exerts its strongest influence during winter (Hurrell 1995; Jones et al. 1997). The behaviour of this circulation is hypothesised to depend on the background climate state.

During the Pleistocene, Earth's climate alternated between glacial and interglacial conditions with a predominant

✉ Deepak Kumar Chinnaswamy
deepak-kumar.chinnaswamy@tu-braunschweig.de

1 CCEHN - Institute of Geosystems und Bioindication, Technische Universität Braunschweig, Braunschweig, Germany

2 Institute of Coastal Systems - Analysis and Modeling, Helmholtz-Zentrum Hereon, Geesthacht, Germany

3 CCEHN - Institute of Ecology, Leuphana University of Lüneburg, Lüneburg, Germany

4 Historical Anthropospheres Working Group, LeipzigLab, Leipzig University, Leipzig, Germany

5 Department Physical Geography, Institute of Geography, Leipzig University, Leipzig, Germany

6 Max Planck Institute for Meteorology, Hamburg, Germany

Published online: 04 July 2026

periodicity of approximately 100,000 years over the last 800,000 years. This includes the Last Glacial Maximum (LGM: 22–19 ka before present, Yokoyama et al. 2001), characterised by large ice sheets covering North America, Eurasia, Greenland, and Antarctica, and the Last Interglacial (LIG, ~ 129–116 ka before present; NGRIP members 2004; Overpeck et al. 2006; Lang and Wolff 2011), which was the warmest period with minimal ice volume since the Pliocene (~ 5.3–2.6 Ma before present; Burke et al. 2018). In contrast to the substantially different conditions of the LGM, particularly over the northern high latitudes, the LIG exhibited a climate state closer to the present day, with Europe experiencing generally warmer and more humid conditions compared to the cold and dry climate that prevailed during the LGM, especially during boreal summer (e.g., Otto-Bliesner et al. 2021; Kageyama et al. 2021). These strongly contrasting climate states were co-determined by the fluctuation of eustatic sea levels from more than 100 m below (LGM) to several metres above the current state (LIG) (Spratt and Lisiecki 2016; Gibbard and Knudsen 2025). And they provide a natural framework for assessing the robustness and potential state dependence of North Atlantic atmospheric variability and its role in shaping the European climate.

During the LGM, global mean near-surface temperatures were substantially lower than in the present climate. Proxy-based reconstructions and model–data syntheses suggest a cooling of approximately 4–5.5 °C (Annan and Hargreaves 2013, 2015; Tierney et al. 2020; Annan et al. 2022), while PMIP4 model simulations span a broader range of ~ 3.3 to 7.2 °C (Kageyama et al. 2021). The largest temperature changes are over the Laurentide and Fennoscandian ice sheets (Kageyama et al. 2021), primarily driven by major changes in surface height and albedo, which in turn are driven by changes in the orbital configuration (Davis and Brewer 2009). This extensive cooling, particularly over extratropical regions, was pronounced during winters both in models and reconstructions (Izumi et al. 2013; Cleator et al. 2020), and was associated with enhanced temperature seasonality. PMIP4 simulations project a decrease in mean annual precipitation relative to pre-industrial (PI) conditions, most pronounced within storm track-dominated regions, alongside a localised increase in precipitation over the Iberian Peninsula (Kageyama et al. 2021).

In contrast, the LIG was generally warmer than the pre-industrial period by globally about 1.9 °C (Turney and Jones 2010), with elevated sea surface temperatures (SSTs) across the North Atlantic and mid-latitude Europe (McKay et al. 2011; Hoffman et al. 2017). Summer temperatures in mid-latitude Europe were substantially higher (about 6 °C). PMIP4 LIG simulations forced at 127 ka (hereafter LIG127k) are in good agreement with proxy reconstructions across Scandinavia, northern Europe, and the North Atlantic for temperature and across the northern hemisphere continents for precipitation patterns (Otto-Bliesner et al. 2021).

During the LGM, European and mid-latitude North Atlantic climate changes were strongly influenced by shifts in atmospheric circulation patterns, particularly during winter (Pausata et al. 2011; Hofer et al. 2012). Ice-sheet–induced southward displacement of frontal zones, leading to cold North Atlantic SSTs and warmer SSTs along the southern continental margin through the eastward diversion of the North Atlantic Current (Broccoli and Manabe 1987; Roe and Lindzen 2001; Löfverström et al. 2014; Martin-Garcia 2019). These SST changes substantially modified temperature gradients, precipitation patterns, and atmospheric circulation during the LGM (Martin-Garcia 2019; Kageyama et al. 2021). Conversely, during the LIG127k, increased shortwave solar radiation in the Northern Hemisphere, driven by orbital changes, was the dominant external forcing (Berger 1978; Yin and Berger 2015). This resulted in substantial warming of northern high-latitude land masses (CLIP members 2006; Otto-Bliesner et al. 2006, 2021; Velichko et al. 2008).

Building on these contrasting climate backgrounds, we focus on the atmospheric variability over the North Atlantic–European sector. The leading modes of (sea level pressure) variability are the North Atlantic Oscillation (NAO), the East Atlantic pattern (EA), and the Scandinavian pattern (SCA), which together largely govern European winter climate (Comas-Bru and McDermott 2014; Hall and Hanna 2018). The NAO is often defined by the sea-level pressure (SLP) difference between Iceland and the Azores (Hurrell 1995; Jones et al. 1997; Cropper et al. 2015) and is more robustly captured using an Empirical Orthogonal Functions (EOF) based approach (Hurrell and Deser 2009). The positive NAO strengthens westerlies, shifting storm activity north-eastward and leading to mild, wet winters in Northern Europe and cold, dry conditions in the south (Hurrell 1995). The negative phase reverses these effects. The NAO has its highest variance during winter, but during summer the pattern also changes, extending the southern pressure centre into mid-and central Europe (Folland et al. 2009).

Although the NAO primarily represents interannual atmospheric variability, its temporal spectrum extends into interdecadal timescales (Wang et al. 2017; Li et al. 2013; Sun et al. 2015). At interannual timescales, the NAO exhibits a largely simultaneous relationship with the North Atlantic tripole SST pattern (NAT), reflecting direct atmospheric forcing of ocean surface variability (Jing et al. 2020; Yu et al. 2024). In contrast, at decadal and longer timescales, the NAO acts as a precursor to ocean-driven multidecadal climate variability, exhibiting a pronounced lead–lag relationship in which persistent NAO anomalies precede Atlantic Multidecadal Oscillation (AMO) variability by approximately 15–20 years, as identified in both observational and modelling studies (Li et al. 2013; Sun et al. 2015).

The EA, often described as a monopole of high-pressure anomaly west of Ireland (Comas-Bru and Hernández 2018), and the SCA, which is characterised by high pressure over Scandinavia (Barnston and Livezey 1987). The exact locations of the major anomaly for both modes are not consistent, even across different reanalysis datasets (Comas-Bru and Hernández 2018). Moreover, the priority of both modes' switches during summer in the observations and historical model simulations (Hall and Hanna 2018). Climate models generally capture the spatial structure and seasonal variability of these modes, although they may underestimate low-frequency variability and slightly misplace the centres of pressure anomalies (Wang et al. 2017). A common bias among these models is a north-eastward displacement of the NAO dipole centres relative to observational data. However, approximately half of the models do not exhibit a clear eastward displacement of the Icelandic Low anomaly (see Fig. 3 in Wang et al. 2017). The eastward displacement of the NAO dipole is particularly pronounced in the LGM simulation of Justino and Peltier (2005), where the Azores High anomaly is displaced eastward toward the Mediterranean region. This results in an east–west pressure gradient alignment, contrasting with the typical northwest-southeast orientation. Furthermore, under present-day climate conditions, Börgel et al. (2020) proposed that the positive AMO phases shift the Northern pressure centre westward and the Southern pressure centre eastward, with the opposite occurring during negative AMO phases. Additionally, eastward shifts in NAO pressure centres correlate strongly with European climate impacts, particularly over Northern Europe (Beranová and Huth 2008).

Atmospheric variability over the North Atlantic has been extensively studied for the observational period, with a limited number of studies extending into historical and palaeoclimate contexts (e.g., Hurrell 1995; Jones et al. 1997; Justino and Peltier 2005; Cropper et al. 2015; Wang et al. 2017). Examining atmospheric variability across distinct climate states may therefore provide additional insight into the state dependence of dominant modes of variability.

The objective of this study is to quantify and compare atmospheric circulation and the state dependence of the variability patterns over the North Atlantic during the LGM, LIG127k, and PI, and to evaluate how associated changes shape European temperature and precipitation patterns. The paper is structured as follows: Sect. 2 outlines the data and methodology, including climate model simulations and variables analysed. Section 3.2 presents differences in mean climate, atmospheric circulation, and SST across the LGM, LIG127k, and PI periods. Section 3.3 examines variability through EOF and correlation analysis with North Atlantic Ocean indices. Section 3.4 presents EOF regression analyses with the European climate. Section 4 provides a discussion of the results, and Sect. 5 summarises key conclusions and highlights potential directions for future research.

2 Data and methods

2.1 Data

This study utilises model simulations from the Coupled Model Intercomparison Project 6 (CMIP6: Eyring et al. 2016)/Palaeoclimate Modelling Intercomparison Project 4 (PMIP4: Kageyama et al. 2018). The analysis covers three periods: the Last Interglacial (LIG127k), the Last Glacial Maximum (LGM), and the Pre-Industrial (PI) era, with the simulations representing conditions from 21 ka (LGM), 127 ka (LIG127k), and 1850 CE(PI), respectively. Each of these points in time is characterised by different climatic background conditions. As part of PMIP4, all simulations follow PMIP4 guidelines for the boundary conditions. Details regarding the boundary conditions and the experimental setup are mentioned in Kageyama et al. (2017) for the LGM, Otto-Bliesner et al. (2017) for the LIG127k, and Eyring et al. (2016) for the PI period. The details of the CMIP6 forcing used for the simulations of individual periods are given in Table 1.

The models were selected based on the availability of simulations for the PI, LGM, and LIG127k periods. AWI-ESM-1-1-LR (Danek et al. 2020; Shi et al. 2020a, b), MIROC-ES2L (Hajima et al. 2019; Ohgaito et al. 2019; O'ishi et al. 2019), and INM-CM4-8 (Volodin et al. 2019a, b, c) provide outputs for all three periods. CESM2 (Danabasoglu 2019a, Danabasoglu et al. 2019) includes PI and LIG127k simulations, while MPI-ESM1-2-LR (Wieners et al. 2019; Jungclaus et al. 2019) and CESM2-WACCM-FV2 (Danabasoglu 2019b) include PI and LGM. The LIG127k simulation is not available for MPI-ESM1-2-LR and CESM2-WACCM-FV2, and the LGM simulation is not available for CESM2. The models are included to represent a bandwidth of models from different origins. Further details of the models can be found in Kageyama et al. (2021) and Otto-Bliesner et al. (2021).

This study utilises variant label r1i1p1f1 for all model simulations, except for MIROC-ES2L (r1i1p1f2) and CESM2-WACCM-FV2 (r1i2p1f1). To understand and compare the climate over the periods in the context of the questions addressed in this study, we use multiple variables related to SLP, SST, near-surface air temperatures (SAT), precipitation, 10-m wind zonal component, and its meridional component, sea ice concentration, mixed-layer depth, and net downward heat flux into the ocean (labelled as PSL,

Table 1 Forcing details of CMIP6 simulations for LGM, LIG127k, and PI based on Kageyama et al. (2017) for the LGM, Otto-Bliesner et al. (2017) for the LIG127k, and Eyring et al. (2016) for the PI

Period	CO_2 (ppm)	CH_4 (ppb)	N_2O (ppb)	Orbital Parameters $(e, \varepsilon, \varpi)^*$	Ice sheet configuration	Land-sea mask
LGM	190	375	200	e = 0.018994, ε = 22.949°, ϖ = 114.42°	PMIP4-LGM Ice Sheet	modified (Glacial)
LIG127k	275	685	255	e = 0.03937 ε = 24.040°, ϖ = 275.41°	Standard PI	Modern (unchanged)
PI	284.2	808.2	273	e = 0.016764 ε = 23.459°, ϖ = 100.33°	Standard PI	Modern

* $e = Eccentricity, \varepsilon = Obliquity \varpi$ = Longitude of Perihelion

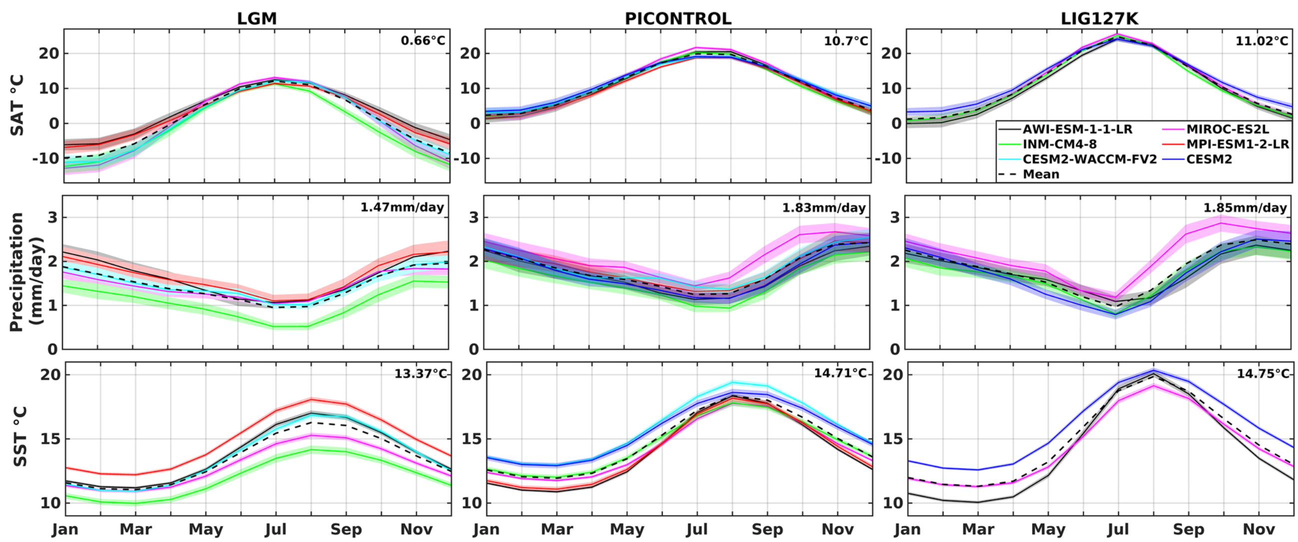

Fig. 1 Monthly 100-year climatology for the European sector (30°N–75°N, 10°W–40°E) of near-surface air temperature (top row), precipitation (middle row), and the North Atlantic sector (20°N–80°N, 90°W–30°E) of sea surface temperature (SST; bottom row). The first, second, and third columns correspond to the LGM, PI, and LIG127k periods, respectively. Each coloured line represents a different model (see legend), the shaded area indicates one standard deviation, and the dashed black line shows the multi-model mean. Note: Climatology includes SST values under sea ice

TOS, TAS, PR, UAS, VAS, SICONC, MLD, and HFDS in CMIP6, respectively).

2.2 Methodology

Atmospheric circulation and SST are critical drivers of temperature, precipitation patterns, and their variability over Europe. For this study, we consider two regions, one covering Europe (30°N–75°N, 10°W–40°E) and a second one that also includes the North Atlantic (20°N–80°N, 90°W–40°E). Surface temperature and precipitation are analysed only over Europe (except for Fig. 1). For other variables, representing the large-scale drivers of the European climate, the domain is extended to the North Atlantic.

The analysis focuses on the winter season (summer is presented in the supplementary information), with seasonal definitions following the modern calendar, without adjustments for changes in seasonal lengths due to variations in eccentricity or the longitude of perihelion. The associated insolation anomalies related to the LIG127ka and LGM can be found in Fig. 1 in Otto-Bliesner et al. (2021) and Fig. 2 in Kageyama et al. (2017). Furthermore, the effects of topographic differences between the periods are not taken into consideration in this analysis. However, the LGM condition has stark differences in topography, and the models consider this. It is important to note that land-sea configurations are vastly different during different periods. In the following, the underlying map of the coastline in all figures represents modern (pre-industrial) conditions.

As the total number of simulated years varies among different models, 100 years of each simulation are analysed for consistency. For the SST analysis, the temperature of the ocean surface's top layer is used, which includes temperatures below sea ice. For the SST-related analyses, the SST is masked for sea ice, unless explicitly stated otherwise. Masking is not applied for the spatial mean in Fig. 1 or for the LGM SST in the INM-CM4-8 model (as data were unavailable). A grid point is considered sea-ice covered when the area fraction of sea ice exceeds 50%. While sea-ice extent is traditionally defined by a 15% concentration threshold, we applied a more conservative 50% threshold to mask grid cells. This choice ensures that the mean SST state and subsequent SST-NAO correlation analyses are based on robust open-ocean signals, minimising the risk of ice-contaminated anomalies influencing the results. Sensitivity checks using thresholds of 25%, 50%, and 75% revealed no substantial large-scale differences in the overall extent of the simulated sea ice in the regions of interest for our analysis.

Among the chosen models, FESOM (AWI-ESM-1-1-LR) uses an unstructured grid (finite element method) for the ocean component, and the SST of AWI-ESM-1-1-LR is interpolated to a 1° × 1° global grid.

Latitude-dependent cosine weighting is applied to account for the variation in grid-cell area with latitude. In the EOF analysis, the square root of the cosine of latitude is applied to the input fields so that the resulting covariance matrix is effectively area-weighted. For spatial mean calculations, cosine latitude weighting is used, which is equivalent to an area average on a regular latitude–longitude grid for Fig. 1.

The EOF analysis (Wilks 2006) is employed to decompose variability into distinct hierarchical modes. In this study, the EOF analysis is applied to SLP, with a focus on SLP-based definitions of the NAO, EA, and SCA.

For the analysis:

1. The seasonal mean SLP is first detrended (x), and the SLP anomaly is calculated.
2. The covariance matrix (C) of the SLP anomaly is calculated as below (spatial weights are adjusted and multiplied by the SLP anomalies prior to the calculation of the covariance matrix).

$$C = \frac{1}{N-1}\sum_{i=1}^{N}\left(x_i - \overline{x}\right)\left(x_i - \overline{x}\right)^T$$

3. The covariance matrix C of the SLP anomaly is decomposed using Singular Value Decomposition (SVD), and the eigenvalues and eigenvectors are extracted.

$$C = \frac{1}{N-1}\sum_{i=1}^{N}\left(x_i - \overline{x}\right)\left(x_i - \overline{x}\right)^T$$

$$SVD\,(C) \Rightarrow C \equiv V\lambda V^T$$

whereas, V is the matrix of eigenvectors, λ is the diagonal matrix of eigenvalues, and $V^T i$ s the transpose V.

To present the EOF maps with units, the EOF maps are multiplied by the square root of the standard deviation of the corresponding principal components. The principal components (PC) are normalised to unit variance by dividing them by their standard deviation.

To relate large-scale atmospheric variability to oceanic conditions, the PCs were correlated with the Atlantic Multidecadal Oscillation (AMO) index and the North Atlantic tripole SST pattern (NAT). The NAT index is defined as a linear combination of area-weighted mean SST anomalies over three regions of the North Atlantic. The positive-polarity region (Box B) is defined over 30°–50°N, 80°–50°W, while two negative-polarity regions are defined over the subpolar North Atlantic (Box A; 55°–65°N, 60°–20°W) and the subtropical eastern North Atlantic (Box C; 15°–30°N, 45°–15°W) (Sun et al. 2015). The NAT index is computed as the difference between the mean SST anomaly in the positive region and the average of the two negative regions as follows:

$$\mathrm{NAT} = \left(SST_B - \frac{(SST_A + SST_C)}{2}\right)$$

representing the canonical NAO-related SST tripole pattern. The AMO index is defined as the area-weighted mean SST anomaly over the North Atlantic basin (0–60°N, 80°W–0°), with the global mean SST removed to isolate internal variability (Trenberth and Shea 2006). To isolate low-frequency variability, the PC and AMO indices are filtered using an 8-year low-pass Lanczos filter. This filtering suppresses interannual variability and highlights decadal-scale fluctuations that are relevant for ocean–atmosphere coupling.

In addition, the spatial structure of atmospheric variability is characterised by tracking and identifying the locations of the dominant pressure centres associated with each mode. To reduce small-scale noise and emphasise large-scale circulation features, the EOF spatial patterns of sea level pressure are smoothed using a moving-average filter before identifying the location of the pressure centres. Pressure centre positions are then defined as the locations of maximum and minimum sea level pressure anomalies in the smoothed EOF patterns.

To understand the influence of the different modes of atmospheric variability, linear regression analysis, based on the ordinary least squares method, is applied. The analysis is performed using the regress function available in MATLAB. The standardised Principal Components (PCs) are used as the predictor or independent variable, and precipitation and surface temperatures are the dependent variables (Y). The linear regression follows the equation below with ϵ as the residual. Only the leading two EOF modes of variability are considered. The regression coefficients and their corresponding statistical significance are plotted in the figures in Sect. 3.4. Only regions indicating statistical significance of more than 95% ($p<0.05$, based on the F-statistic calculated by the regress function in MATLAB) are highlighted.

For instance, the regression of the 1st PC (PC_1) onto the variable surface air temperature (T_{2m}) at a given grid point (n, m) is as follows:

$$Y_{T_{2m}}(n,m) = PC_{slp1} \times \beta(n,m) + \varepsilon(n,m)$$

with β representing the regression coefficient and ϵ the residual for the grid point under consideration. This process is applied to all grid points for SST, surface air temperature, and precipitation.

3 Results

3.1 Seasonal cycle and inter-model spread

The simulated LGM SAT over the European sector (Fig. 1a–c) are lower compared to the interglacials, with LIG127k being the warmest period with average annual temperatures of 11.02 °C (LIG127k), followed by 10.7 °C (PI), and 0.66 °C (LGM). Additionally, greater seasonality during the LIG127k, compared to PI, is captured by all models. However, seasonality is slightly higher during the LGM compared to the LIG127k. Among the models, the warmest mean SAT over Europe is evident in CESM2 (LIG), while INM-CM4-8 tends to simulate the coldest temperatures during LGM. The ensemble monthly mean climatology over the European sector, in December, shows SAT of about −10 °C during the LGM, with mean temperatures below zero for at least six months.

The inter-model spread in SAT during the LGM is substantial, reaching on average 4.26 °C (−1.46 °C to 2.8 °C). This uncertainty is equivalent to 42% of the ensemble-mean difference between LGM and PI (10.04 °C), highlighting significant model uncertainty relative to the total cooling signal. The inter-model differences are less pronounced during PI (1.03 °C) and LIG127k (1.99 °C). Notably, the model spread during the LGM is high, particularly during winter (when variability is highest), with temperatures ranging between −6 °C and −12 °C over the European domain (c.f. Fig. 1). Stemming from the same origins, AWI-ESM-1-1-LR and MPI-ESM1-2-LR show similar values.

The ensemble annual mean precipitation during the LGM over the European sector is 20% lower, averaging 536 mm, compared to 667 mm during PI and 675 mm during LIG127k. However, the lower ensemble mean for the LGM is skewed by the considerably lower precipitation values of INM-CM4-8 (Fig. 1). Excluding INM-CM4-8, the other models display a more concentrated distribution or a higher degree of similarity related to the monthly mean precipitation during the LGM. During interglacial periods, MIROC-ES2L stands out, showing considerably increased precipitation during autumn. In general, the INM-CM4-8 model shows lower precipitation, while MIROC-ES2L tends to produce higher precipitation than other models. The peak precipitation for most models occurs during the Northern Hemisphere winter, except for MIROC-ES2L, which shows peak precipitation during warmer periods, with the maximum shifting towards October.

The spatial mean SST shows higher seasonality for LIG127k, compared to PI and LGM (Fig. 1, third row). Due to the unavailability of sea-ice data for INM-CM4-8-LGM, the SST here also includes SST under sea-ice. The SST minimum occurs during February and March. The LGM SST spatial mean is approximately 1.35 °C colder than PI and LIG127k. Interestingly, the winter SSTs from MPI-ESM1-2-LR and AWI-ESM-1-1-LR are warmer during the LGM than PI. This counterintuitive result likely stems from a methodological artefact related to sea-ice expansion, as the SST analysis here includes data from beneath the sea ice. Under extensive LGM sea-ice cover, the underlying ocean temperature remains fixed at the freezing point, whereas open-ocean temperatures in the PI may exhibit higher variability. The insulation effect of the sea-ice layer thus biases the spatial average. Seasonality in SST is most pronounced during LIG127k, with a larger model spread in winter, similar to SAT. Additionally, the model spread remains uniform across all months during the LGM, while LIG127 winters exhibit the largest spread.

Concerning near-surface temperatures, winters exhibit greater variability than summers, with the highest variability occurring during LGM winters. Compared to PI, winter variability is slightly higher for LIG127k. In contrast, summer variability during LGM shows a similar range during both LIG127k and PI. Among the models, INM-CM4-8 displays the greatest differences for the LGM. Overall, the AWI-ESM-1-1-LR and MPI-ESM1-2-LR models show a warmer mean state during LGM, in terms of both surface air temperatures and SST, compared to other models.

3.2 Winter climatology and background circulation

This section examines the spatially resolved background climatological differences across the studied periods, focusing on near-surface air temperature and precipitation. In addition, sea level pressure, surface winds, North Atlantic sea-surface temperatures, as well as sea-ice distribution, are shown to characterise the large-scale circulation and oceanic background state. Summer results are presented in the supplementary information.

3.2.1 Near-surface air temperatures

The spatial mean of SAT during winter (Fig. 2) is lower overall in all the regions of Europe during LGM compared to PI. The strongest cooling occurs over areas covered by ice sheets, which exhibit substantially colder conditions relative to PI. This is largely due to the high altitude of the ice sheets (lapse rate effect), in addition to their high albedo. Notably, AWI-ESM-1-1-LR and MPI-ESM1-2-LR (Fig. 2a, b) show warmer temperatures than other models, with local anomalies at individual grid points reaching up to ~4 °C. The pronounced surface cooling is also confined to the land surface. In other models, the cooling extends into the ocean towards the North of Europe. During the LGM, all models exhibit temperatures at least 5 °C lower over most of Europe, except over the Iberian Peninsula. Similarly, during LIG127k, all regions are colder compared to PI, except for areas around the Norwegian Sea in CESM2. Landmasses are generally colder, with the coldest temperatures observed over Eastern Europe, which is similar to the warming pattern during summers (Fig. S1).

3.2.2 Seasonal precipitation

Precipitation differences (Fig. 3) indicate lower seasonal rainfall values by about 50–100 mm (seasonally accumulated precipitation) during LGM, compared to PI, except for AWI-ESM-1-1-LR, where the precipitation increased by about 20–100 mm. All models show an increase in precipitation during the LGM over Iberia, except for INM-CM4-8 and MIROC-ES2L. The maximum decrease in precipitation is about 100 mm over Scandinavia. The wet anomalies extend towards central Europe in AWI-ESM-1-1-LR, while other models show negative precipitation anomalies over the largest part of Europe. During the LIG127k, all regions of Europe show less seasonally accumulated precipitation (~ 10–20 mm), except over Iberia (for MIROC-ES2L and CESM2). The anomalies are smaller for the LIG127k than during the LGM.

3.2.3 Sea level pressure and near-surface wind

The spatial mean surface pressure fields (Fig. 4) over Europe and the North Atlantic exhibit increased values during LGM compared to PI, with a rise of about 20 hPa in winter relative to PI and LIG127k. However, the differences between the latter two are very low. This increase is attributed to the high elevations and cold temperatures over the ice sheets. The difference is largest up to 25 hPa for AWI-ESM-1-1-LR (Fig. 4a). However, the SAT difference over the ice sheets in AWI-ESM-1-1-LR is lower compared to the other models (Fig. 2a). Regions over the ice-sheet and the region between the pressure centres, where the storm track is located, indicate the maximum increase, while over the region of the Azores High, a smaller increase is evident. In the AWI-ESM-1-1-LR model (Fig. 4a), the difference over the Azores High (LGM-PI) is 2–3 times stronger than in other models. The MIROC-ES2L model shows a southward shift in the Icelandic Low by about 5–10° during LGM, and approximately 10° during PI, compared to other models. Due to the increased pressure gradient between the high-pressure and low-pressure centres, the surface zonal

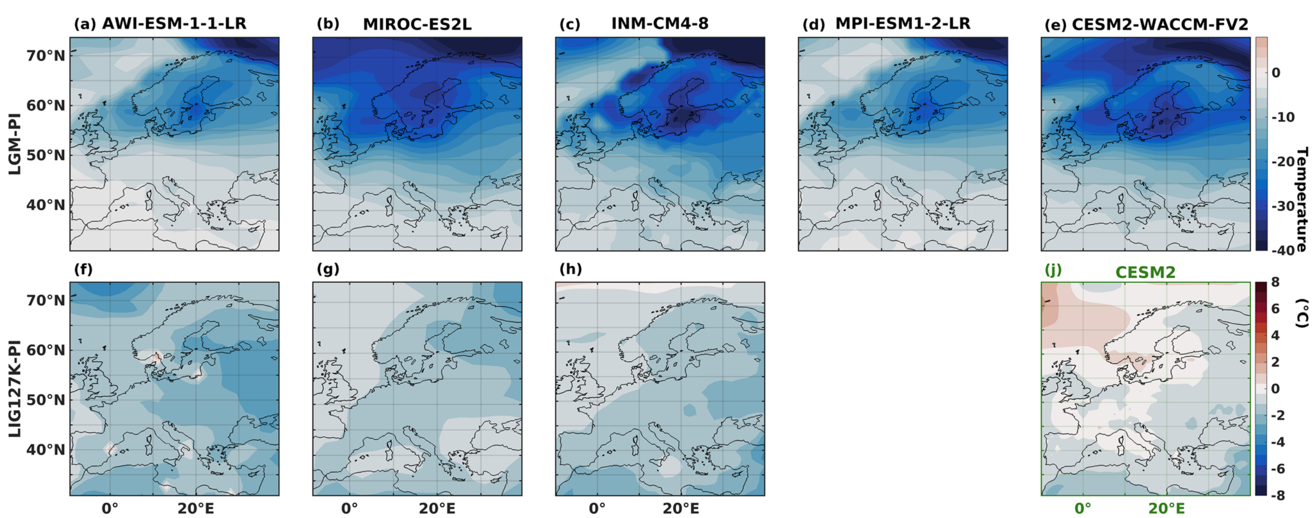

Fig. 2 Differences in mean near-surface air temperature for December–February: LGM minus PI (top row, panels **a**–**e**) and LIG127k minus PI (bottom row, panels **f**–**j**). Each column corresponds to a different CMIP6 model, except for the rightmost column, which shows CESM2-WACCM-FV2 in the top panel and CESM2 in the bottom panel. Colour bars are adjusted between rows to reflect differences in magnitude. Units: °C

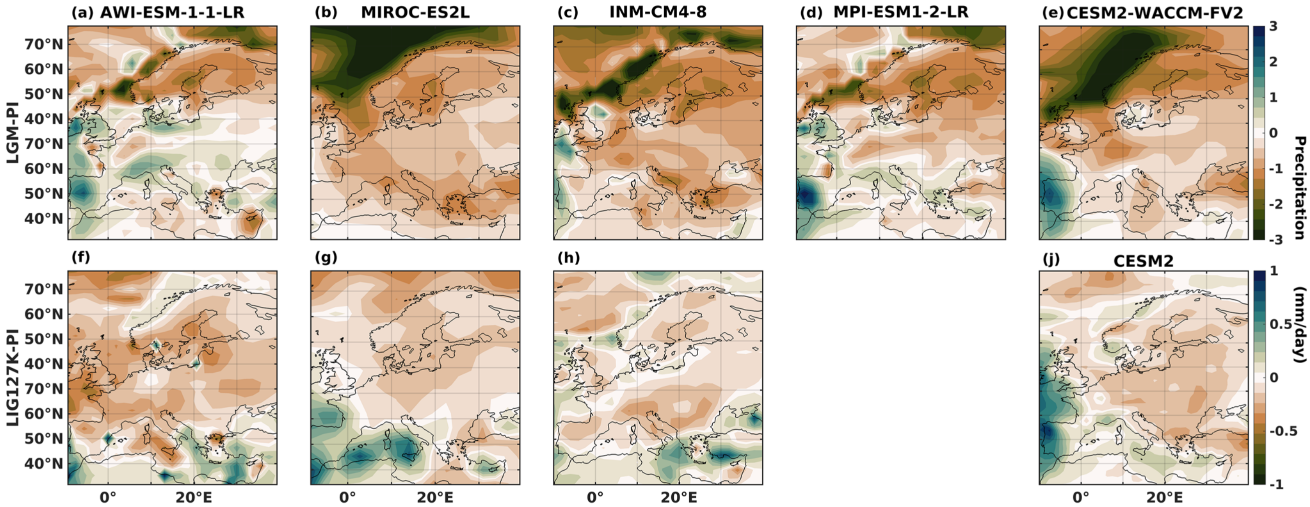

Fig. 3 Differences in daily precipitation for December–February: LGM minus PI (top row, panels **a**–**e**) and LIG127k minus PI (bottom row, panels **f**–**j**). Each column corresponds to a different CMIP6 model, except for the rightmost column, which shows CESM2-WACCM-FV2 in the top panel and CESM2 in the bottom panel. Colour bars are adjusted between rows to reflect differences in magnitude. Units: mm/day

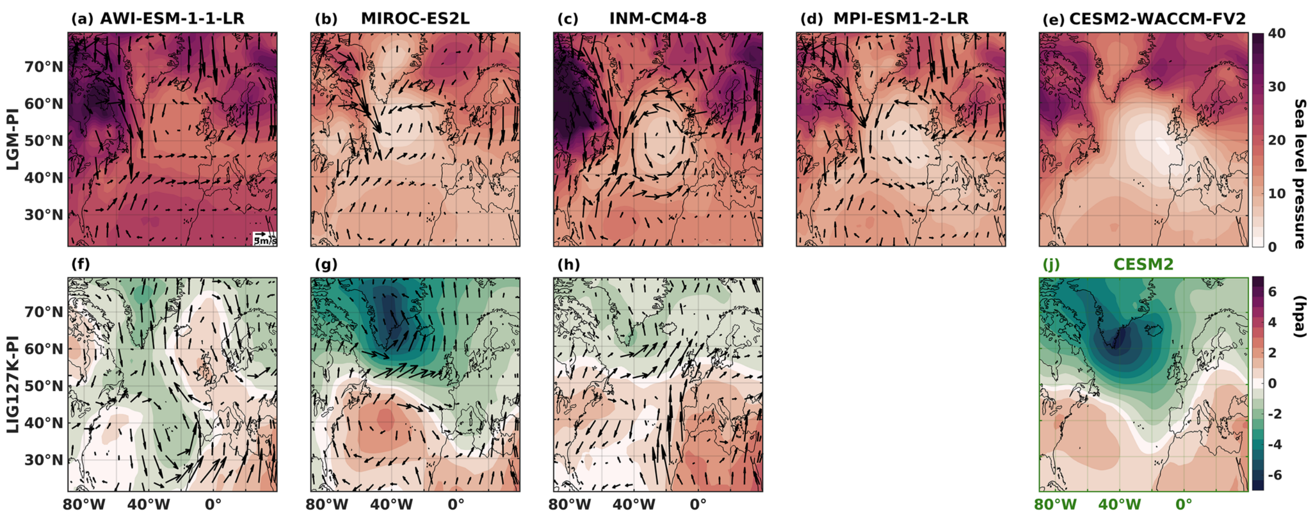

Fig. 4 Differences in mean sea level pressure (colour shading) and surface winds (arrows*) for December–February: LGM minus PI (top row, panels **a**–**e**) and LIG127k minus PI (bottom row, panels **f**–**j**). Each column corresponds to a different CMIP6 model, except for the rightmost column, which shows CESM2-WACCM-FV2 in the top panel and CESM2 in the bottom panel. Colour bars are adjusted between rows to reflect differences in magnitude. *Arrows are scaled according to the maximum wind speed across all subplots; a reference arrow of 5 m/s is shown in the bottom-left corner of panel (a)

winds over the region in the middle of the pressure centres are also intensified.

The main topographic difference between the LGM and PI is the presence of extensive and high-elevation ice sheets (Laurentide and Fennoscandian) during the LGM. These ice sheets influenced the LGM pressure systems by acting as orographic barriers along with the cold temperatures over high-elevation regions. The changes in the pressure systems contribute to the southward shift of the storm track and a more zonal wind flow in the central Atlantic.

In winter, the Icelandic Low extends northward over Scandinavia and the Norwegian Sea during the interglacial periods. The presence of ice sheets during the LGM creates high pressure over these regions. In addition, low pressure expands southward over southern Europe, in conjunction with a comparatively weaker Azores High during the LGM. In contrast, during warm periods, a weaker high pressure is located over western and southern Europe. These differences in climatological pressure patterns alter the orientation of the surface winds over regions between the pressure centres, where winds are mostly zonal. During interglacial periods, the surface winds surrounding the low-pressure system extend into northern Europe via the British Isles. During the LGM, the zonal winds were deflected south over Iberia due to the presence of high pressure over northern Europe, and according to shifts and deflections of the low-pressure systems. The circulation becomes more meridional over the British Isles, without extending into northern Europe. In addition, during LGM, the presence of low pressure over central and southern Europe, along with elevated high pressure over the ice sheets, generates stronger catabatic winds towards the south (Fig. 4a–e). This flow significantly lowers central European temperatures and could explain the gradual temperature rise from the ice sheets to the Mediterranean during winter (Fig. 2a–e), compared to summer (Fig. S1a–e in the supplementary information).

The spatial distribution of the sea level pressure difference (LIG127k-PI), shown in the bottom panel of Fig. 4, reveals a large-scale dipole pattern, encompassing the entire North Atlantic realm. This dipole is characterised by a negative pressure anomaly in the north and a positive anomaly in the south compared to PI, leading to stronger zonal winds over the central North Atlantic. However, the patterns are not consistent across models. In general, northern Europe and specific regions of western Europe are characterised by relatively low pressure, albeit with a high intra-model heterogeneity.

3.2.4 Sea ice extent and sea surface temperatures (SST)

Sea ice extent during the LGM is most pronounced in MIROC-ES2L and CESM2-WACCM-FV2 (Fig. 5b, e), stretching southward over Newfoundland into the Labrador Sea region. In contrast, the sea-ice cover in AWI-ESM-1-1-LR and MPI-ESM1-2-LR (Fig. 5a, d) is less extensive, largely due to warmer SSTs extending further north into the Norwegian Seas. The major difference in sea ice representation is located in the region from the coasts of the British Isles and Norway. Interestingly, AWI-ESM-1-1-LR shows a sea ice-free area over the northern parts of the North Sea, which contrasts with other models. The spatial SST patterns over the North Atlantic Ocean during the LGM reveal significantly reduced temperatures compared to PI, except for a central North Atlantic region in MPI-ESM1-2-LR (Fig. 5d) and AWI-ESM-1-1-LR (Fig. 5a). This same area in MIROC-ES2L (Fig. 5b) does not exhibit a warm bias but shows the lowest cold bias. This region aligns with the storm track, where stronger zonal winds prevail. INM-CM4-8 and CESM2-WACCM-FV2 (Fig. 5c, e) show considerably colder SST compared to AWI-ESM-1-1-LR, MPI-ESM1-2-LR and MIROC-ES2L (Fig. 5a, b, d).

During the LIG127k (Fig. 5f, j), the sea ice extent is small and confined to regions close to Greenland. While the SST was cooler than during the PI, a warm anomaly is observed along the East Greenland Current. This warm anomaly is stronger and spatially extended in the CESM2 model (Fig. 5j) as far south as 50°N and also to Scandinavia in the north. The warming during the LIG127k and the cooling during the LGM are both more pronounced in the CESM2 models.

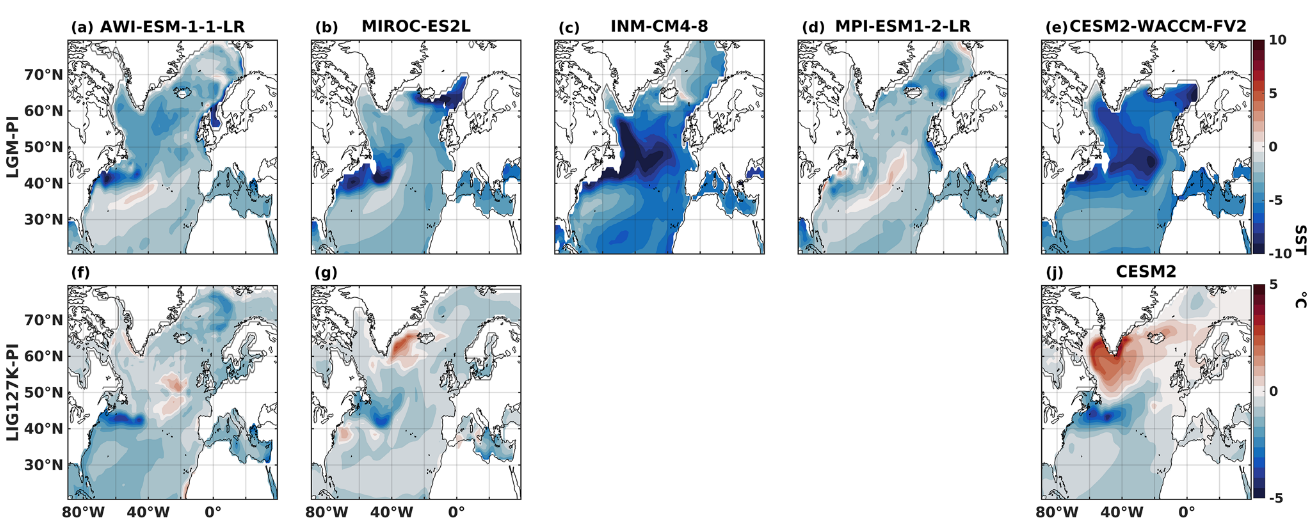

Fig. 5 Differences in mean sea surface temperatures (SST) for December–February: LGM minus PI (top row, panels **a**–**e**) and LIG127k minus PI (bottom row, panels **f**–**j**). Each column corresponds to a different CMIP6 model, except for the rightmost column, which shows CESM2-WACCM-FV2 in the top panel and CESM2 in the bottom panel. Colour bars are adjusted between rows to reflect differences in magnitude. A grey contour line marks the boundary between the ocean (where SST is plotted) and both land and sea ice, and is shown only for latitudes above 50°N. Units: °C. Note: The bottom right panel (j) uses CESM2 due to missing CESM2-WACCM-FV2 data

3.3 Atmospheric variability and its teleconnections (to European near-surface climate)

3.3.1 Leading modes of atmospheric variability

The following section presents the dominant modes of winter atmospheric variability in surface pressure (SLP) and their differences across the different periods and models. Their climatic drivers and impacts are investigated through correlation analyses with ocean indices and linear regressions of the principal components onto near-surface air temperature and precipitation.

The EOF analysis of North Atlantic winter SLP reveals that the first two leading modes account for more than 50% of the total variability, increasing to 60% during the LGM. The North Atlantic Oscillation (NAO) emerges as the dominant pattern of SLP variability across all models and for all periods (Fig. S5), followed by the East Atlantic pattern (EA), except for AWI-ESM-1-1-LR PI (Fig. S5b2), where the second mode is the Scandinavian Pattern (SCA). As EOFs represent standing modes with arbitrary sign, all the discussion focuses on the positive phase of the respective modes (see Methods). The individual patterns of each model and period are presented in the supplementary (Fig. S5), while the ensemble patterns and certain pattern statistics are presented and discussed in the following section.

The ensemble-mean leading EOF patterns of SLP for all three periods display a canonical NAO-like dipole, characterised by a negative pressure anomaly over the subpolar Iceland–Greenland sector and a positive anomaly over the subtropical North Atlantic (Fig. 6a–c). NAO's subpolar low anomaly is narrower and stronger compared to the subtropical high anomaly, with the differences being more pronounced during the LGM. The amplitude of the anomalies and dipole strength are narrower and stronger during the LGM compared to PI, while they are weaker during the LIG127k. Particularly, the subtropical high-pressure anomaly during LIG127k is considerably weaker, weakening the dipole strength. The shaded region in Fig. 6a–c indicates regions of intermodal disagreement, which are the regions away from the core dipole anomalies. For nine out of twelve inter-period model combinations, pattern correlations exceed 90%. Lower correlations occur for INM-CM4-8 (PI–LGM and LGM–LIG127k) and MPI-ESM1-2-LR (LGM–PI). In general, LIG127k–PI correlations are higher, whereas LGM–PI correlations are lower.

The locations of the NAO pressure centre (Fig. 6d) show considerable shifts between periods. During LIG127k, both the centres linked to the subtropical high-pressure anomaly and subpolar low anomaly shift westward, whereas during the LGM, both centres shift southward compared to PI. Additionally, the LGM shows a longitudinal shift, with the

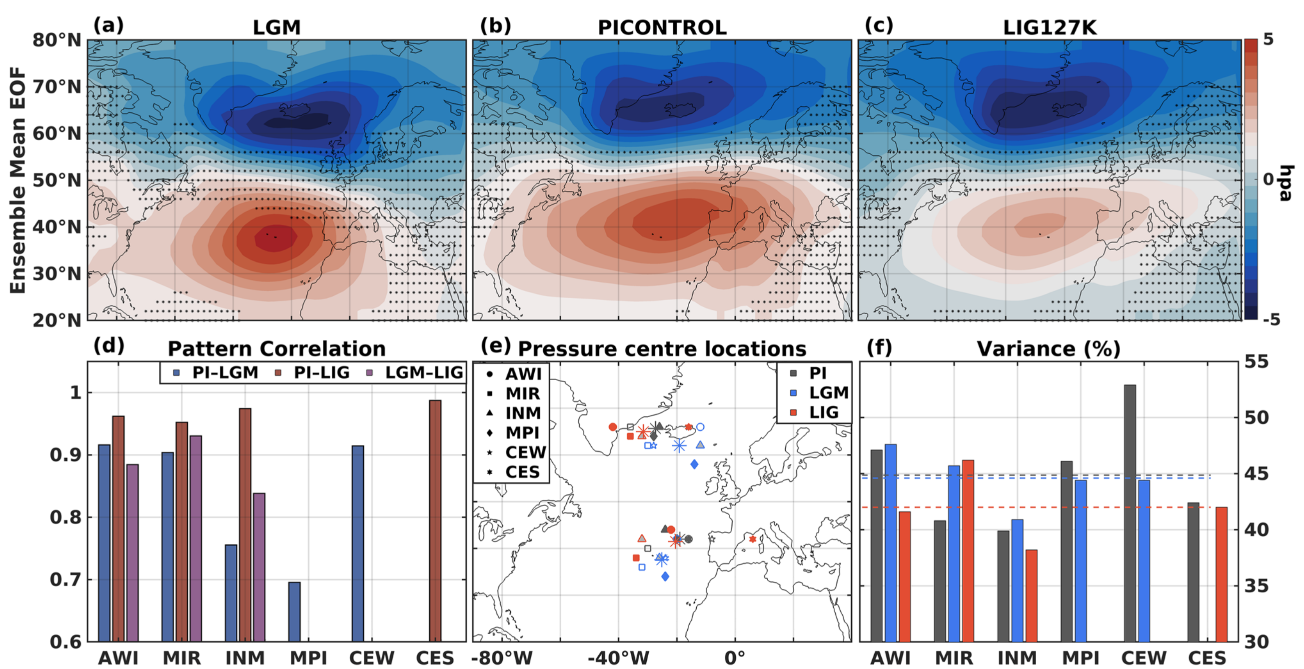

Fig. 6 Ensemble-mean EOF of sea-level pressure (SLP) associated with the North Atlantic Oscillation (NAO) for **a** LGM, **b** PICONTROL, and **c** LIG127k. **d** Pattern correlation between the EOF patterns across different periods for each model. **e** Locations of NAO pressure centres (see Methods) for different periods and models; solid markers denote periods dominated by a positive AMO phase, while open markers indicate negative AMO phases. **f** Explained variance of the leading EOF mode for individual models, grouped by period; colours follow the legend shown in panel (e)

subtropical high shifting westward and the subpolar low shifting eastward.

The variance represented by the NAO (Fig. 6f) ranges from 38.2% (INM-CM4-8-LIG127k) to 52.9% (CESM2-WACCM-FV2-PI), with the LGM generally showing a slightly higher degree of variance, except for MPI-ESM1-2-LR and CESM2-WACCM-FV2. During the LIG127k, the variance is slightly lower compared to PI, except for MIROC-ES2L.

For both positive and negative NAO events (PC exceeding ± 1 standard deviation), each model simulates approximately 20 events each out of 99 winters, with slight variations in the difference between the total number of positive and negative events (ranging from 0 to 4 events). There are no consistent tendencies favouring either positive or negative phases across different periods.

The second mode of variability is related to the EA, characterised by a high-pressure anomaly west of Ireland, surrounded by low-pressure anomalies ranging from the subtropical Atlantic to Northern Europe. In most models, this mode emerges as the second leading mode (Fig. S5). The variance represented by EA ranges between 13.3% (CESMW-PI: Fig. S5n2) and 25% (MPI-ESM1-2-LR-LGM: Fig. S5j2), respectively, with lower values during PI. Notably, in the AWI-ESM-1-1-LR PI (Fig. S5b2) simulation, the second mode represents the SCA, characterised by a high-pressure anomaly over Scandinavia. Unlike the NAO, which remains fairly consistent across periods, the EA pattern shows less spatial consistency and greater structural differences between the different periods. During the PI, the pressure centre locations are consistent across the models, except for CESM2. In all models, the locations of the pressure centres show a south-eastward (LGM) and eastward (LIG127k) shift, making the spatial pattern less uniform.

Overall, the first two modes of variability, NAO and EA, represent dominant interannual variability across all the periods and models, with subtle but important shifts in their spatial structures and variances represented by the individual patterns during the LGM and LIG127k, respectively. These shifts reflect changes in atmospheric circulation patterns, potentially influencing and shaping temperatures and precipitation patterns across Europe.

3.3.2 Association of the NAO with Ocean Indices

Based on the EOF analysis, the corresponding Principal Components (PCs) are used in the following to decipher and identify potential lead-lag relationships with selected North Atlantic Ocean-based indices. The ocean-based indices are related to the Atlantic Multidecadal Oscillation (AMO), the North Atlantic Tripole (NAT), the downward surface heat flux into the ocean (HFDS), and the mixed layer depth (MLD). For the AMO, the model-mean lead-lag correlation of the NAO PC and AMO index shows a positive peak correlation with the NAO (PC) leading AMO by ~ 4 years during the LIG127k and PI. The LIG127k additionally shows a negative peak with AMO leading the NAO (PC) by ~ 5 years. However, large inter-model spread substantially weakens the multi-model mean signal. During the LGM, although the mean suggests a positive peak with the NAO leading by ~ 3 years, the model spread is even larger, rendering the mean correlation inconclusive. Overall correlation amplitudes remain low, likely reflecting the combined effects of 8-year low-pass filtering and the limited sample size (99 winters).

In contrast, the NAO (PC) and the NAT exhibit a robust and physically consistent relationship. All models and periods display a peak positive correlation between the NAT and the NAO (PC) at zero-year lag, consistent with instantaneous atmospheric forcing of SST tripole patterns by the NAO. CESM2-WACCM-FV2 during PI is the only exception, showing a negative peak. Correlation amplitudes are comparable between LIG127k and PI but stronger during the LGM, with MPI-ESM1-2-LR indicating the highest amplitudes. The intermodal agreements are limited to lead–lag times within ± 3 years, beyond which disagreements rapidly increase.

Monthly lead–lag correlations further support this interpretation, showing a rapid strengthening of the NAO–NAT relationship following December NAO events, peaking during January–February, and subsequently decreasing in the following months. This seasonal evolution is consistent across models and periods, except for CESM2-WACCM-FV2 during PI. Inter-model spread is smaller during LIG127k and PI than during the LGM (Fig. 7).

The simultaneous (lag-0) correlation between the net downward surface heat flux into the ocean (HFDS) and the NAO PC (Fig. S7) exhibits a basin-scale tripole-like structure across the North Atlantic, with positive correlations in the mid-latitudes flanked by negative correlations in the subtropical and subpolar regions. This pattern is present in all periods but is notably stronger and more spatially coherent during the LGM. During the PI and LIG127k, the central positive correlations extend farther north into the Norwegian Sea, while the northern negative anomaly reaches toward Iceland. The spatial structure is highly similar between the PI and LIG127k across most models. Statistically significant correlations dominate the major pattern in all periods, except for the CESM2-WACCM-FV2 PI simulation, which exhibits a low and more heterogeneous correlation pattern.

The simultaneous (lag-0) correlation between mixed layer depth (MLD) and the NAO PC (Fig. S8) reveals a large-scale meridional dipole across the North Atlantic,

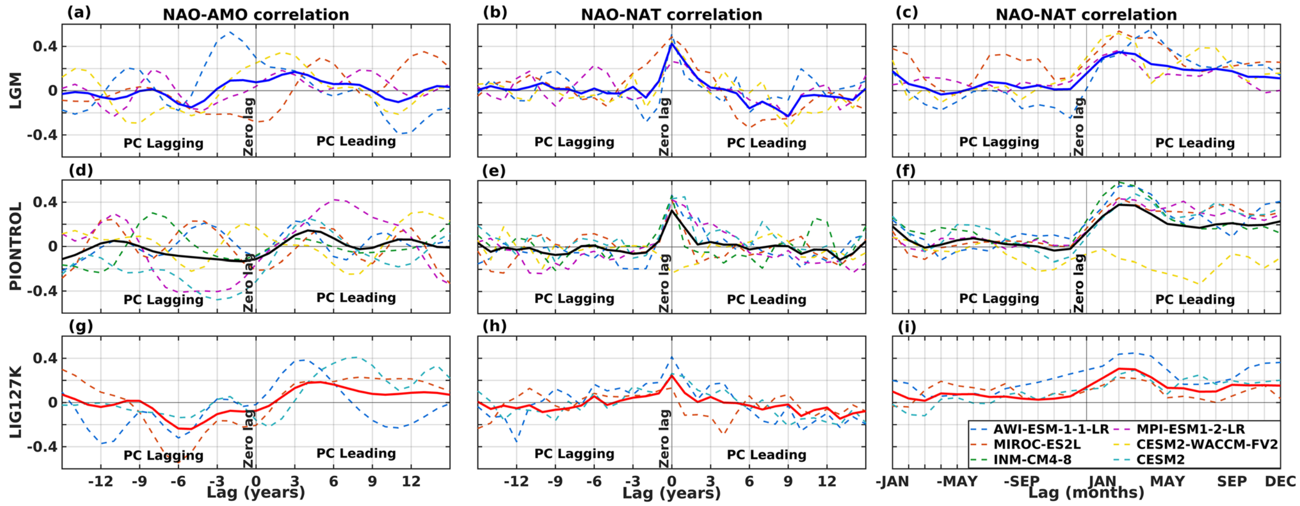

Fig. 7 Relationship between Atlantic Multidecadal Oscillation (AMO), North Atlantic Oscillation (NAO), and North Atlantic temperature (NAT) variability across different climate periods. Panels (**a–c**) show the LGM, panels (**d–f**) the LIG, and panels (**g–i**) the PICONTROL. The first column (a, d, g) shows lead–lag correlations between the AMO index and NAO principal component (PC), both filtered using an 8-year low-pass filter. The second column (b, e, h) shows the correlation between the NAO (PC) and the NAT. The third column (c, f, i) shows correlations between the winter (DJF) NAO (PC) and the monthly NAT index from January (−), before the NAO event, to December (+), after the event. Solid lines indicate the ensemble mean, while dashed lines represent individual models. The legend for the individual models is provided in panel (i)

characterised by deeper mixed layers in the subpolar region and shallower mixed layers in the subtropical Atlantic. This pattern is evident in all climate states and across most models, but is strongest and most spatially coherent during the LGM. In the PI and LIG127k simulations, the structure remains similar, with deep MLD anomalies extending into the eastern subpolar North Atlantic and parts of the Nordic Seas. The spatial correspondence between PI and LIG127k is high, indicating comparable NAO–MLD coupling under interglacial conditions. Statistically significant correlations dominate the main pattern in all periods, except for the CESM2-WACCM-FV2 PI simulation, indicating weak and heterogeneous correlations.

3.4 Teleconnections between atmospheric circulation and North Atlantic SST, temperature, and precipitation over Europe

In the following subsections, we use the EOF results from Sect. 3.3.1 to investigate the relationship between the leading modes of SLP variability and near-surface air temperatures and precipitation over Europe across different models and periods.

3.4.1 Relation between atmospheric circulation and near-surface temperature fields

The regression coefficients of the leading PCs of sea level pressure onto near-surface air temperatures reach 1 °C per one standard deviation of the PCs over the ocean and around 0.6 °C over land (Fig. 8). The regression patterns show a dipole response, with the positive (negative) phase of the NAO resulting in a warming (cooling) over northern and north-western Europe, and a cooling (warming) over southern Europe. The fingerprint of this dipole pattern between northern and southern Europe gets weaker downstream into the eastern parts of Eurasia. The regression coefficients are weaker during the LGM, especially over northern Europe, but are statistically significant at the 95% level. The sensitivity of temperatures to the PCs is significantly amplified during interglacials. Specifically, coefficients over the north-west are nearly three times the LGM values, while those in the south are twice as high. Although the variance represented by the NAO for LGM is slightly higher than during the interglacial periods, the regression coefficients on surface temperature are comparatively weaker. However, during LGM, MPI-ESM1-2-LR (Fig. 8j1) shows a monopole warming instead of a dipole response, and INM-CM4-8 displays a dipole oriented along a north-east to south-west.

Across the periods, the second mode of variability of winter surface pressure is predominantly related to a monopole, and its positive phase, characterised by high-pressure west of Ireland, leading to a cooling over the European sector from the south, causing very strong negative temperature anomalies over the Mediterranean. This anomaly is stronger than that of the NAO, most likely because of the advection of cold air masses from the North into central and southern Europe. Positive regression coefficients can only be seen in the region of the British Isles and the north-western coast of Europe in CESM2 (Fig. 8l2, o2), CESM2-WACCM-FV2

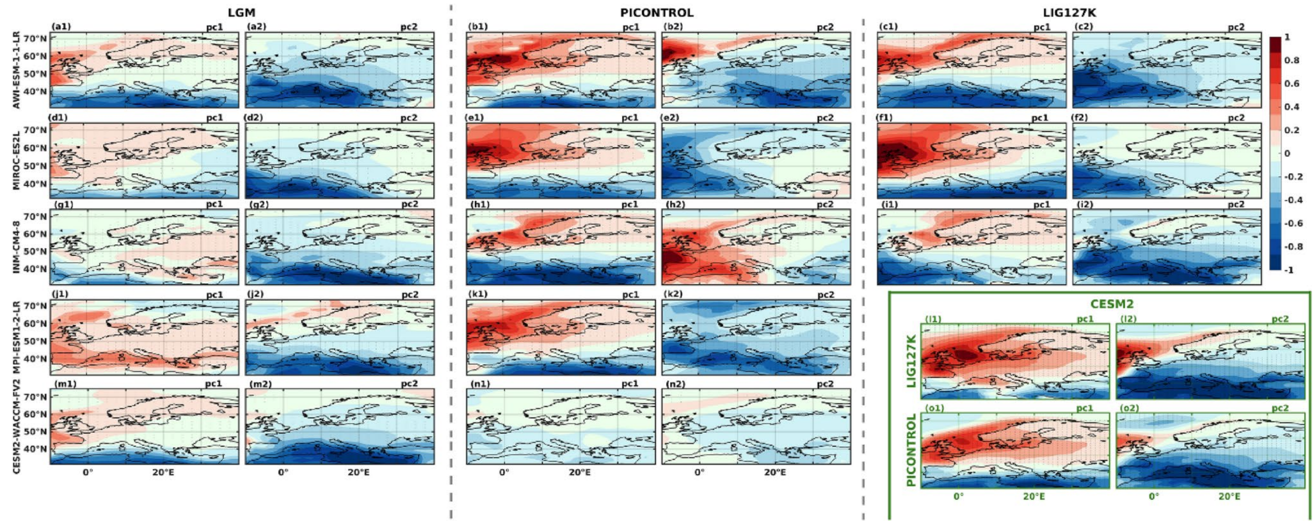

Fig. 8 Regression of principal components (PCs) of December–February EOF patterns in Fig. S5 onto winter near-surface air temperature over Europe. Dots represent regions where the regression is significant at the 95% confidence level. The colour bar shows the regression slope in °C per one standard deviation of the PCs. For each model, regression coefficients of the first two dominant modes are shown in two adjacent columns (e.g., a1 and a2 for Modes 1 and 2 of the first model). Mode numbers are indicated at the top of each subplot. Sign conventions for the EOF patterns are adjusted to represent the positive phase. *Note that due to missing data, the last four columns of the bottom row show CESM2-LIG127k (l1 & l2) and CESM2-PI (o1 & o2) patterns

(Fig. 8m2, n2), AWI-ESM-1-1-LR-PI (Fig. 8b2) and MPI-ESM1-2-LR-LGM (Fig. 8j2). The cooling over the Mediterranean is stronger during LIG127k. The positive phase of EA brings in a significant amount of cooling over southern and western Europe. Over northern Europe, the impacts of both modes are very weak. The regression coefficients of CESM2 are stronger for both modes, similar to its pronounced EOF loading (Fig. S5). In contrast, the regression coefficients of both modes, shown by CESM2-WACCM-FV2 for PI, and mode one of INM-CM4-8 for LGM, are very low compared to other models.

3.4.2 Relation between atmospheric circulation and precipitation fields

The regression coefficients of the leading SLP-PCs onto the precipitation fields indicate that the positive phases of both the NAO and EA patterns are associated with a reduction in precipitation over the continent (Fig. 9). In general, a positive NAO-related precipitation pattern indicates a tripole response, with the positive values over northern and southern Europe and the Mediterranean Sea, and negative values in central and western Europe. For continental areas, the regression pattern shows reduced precipitation over Europe, except for Scandinavia. The regression patterns indicate the highest coefficients for precipitation over northern Europe over the ice sheet during the LGM. This localised increase is likely driven by the mechanical forcing of the westerlies encountering the steep topography of the ice sheet, resulting in enhanced orographic lifting on the windward side. This is unique to LGM and is one of the most noticeable differences among the periods. During the LGM, a northward extension of the negative regression coefficients is evident. The pattern related to EA resembles a northward shift in the NAO response, with negative precipitation anomalies covering Europe, with some positive anomalies in the south. The difference for AWI-ESM-1-1-LR and INM-CM4-8 PI mode 2 of SLP (Fig. 9b2, h2) also shows different patterns in its influence over precipitation, with the majority of regions showing a reduction in precipitation. A similar pattern is indicated for surface air temperatures. In this case, CESM2-WACCM-FV2-PI shows a weaker response to both modes. In general, all patterns are statistically significant over most of the region, except for specific regions of the EA-related precipitation patterns (Fig. 9d2, k2, f2).

The primary focus of this study is on atmospheric variability, which peaks during boreal winter for the dominant modes over the North Atlantic–European sector. Summer circulation and climatology are therefore not discussed in the main text. To maintain a clear focus and reasonable manuscript length, the figures of the summer climatological fields and circulation patterns, along with a summary, are provided in the supplementary information.

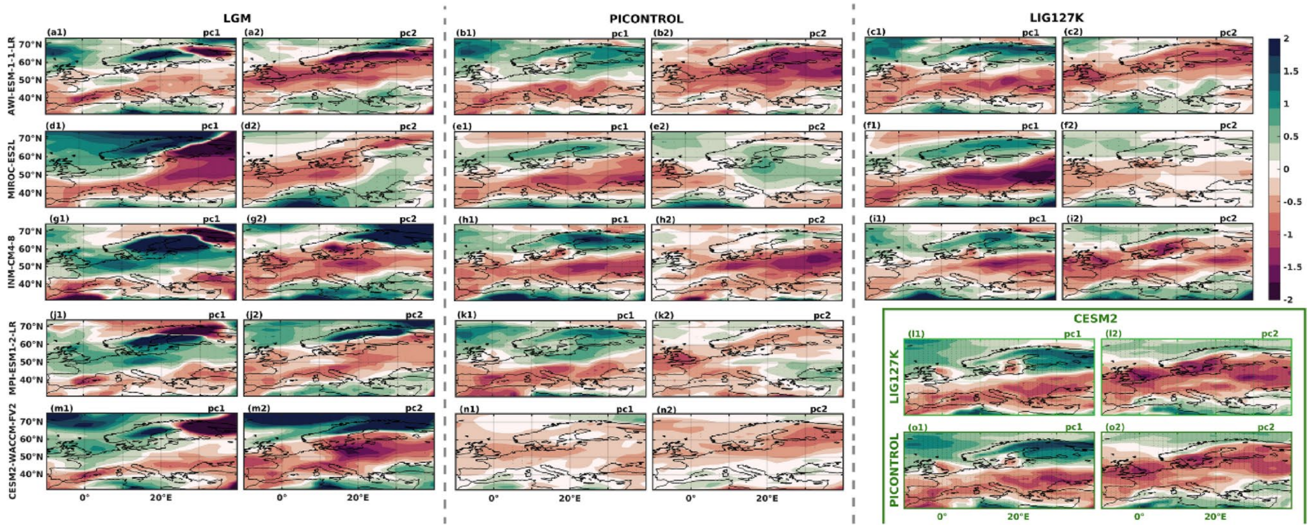

Fig. 9 Regression of principal components (PCs) of December–February EOF patterns in Fig. S5 onto precipitation over Europe. Dots represent regions where the regression is significant at the 95% confidence level. The colour bar shows the regression slope in mm/day per one standard deviation of the PCs. For each model, regression coefficients of the first two dominant modes are shown in two adjacent columns (e.g., a1 and a2 for Modes 1 and 2 of the first model). Mode numbers are indicated at the top of each subplot. Sign conventions for the EOF patterns are adjusted to represent the positive phase. *Note that due to missing data, the last four columns of the bottom row show CESM2-LIG127k (l1 & l2) and CESM2-PI (o1 & o2) patterns

4 Discussion

4.1 LGM and LIG mean state changes

The GM is characterised by the presence of extensive continental ice sheets and colder SST across the North Atlantic. The high elevation and large spatial extent of the Laurentide and Fennoscandian ice sheets fundamentally alter the large-scale atmospheric circulation by modifying the planetary wave structure and introducing stationary waves, promoting persistent anticyclonic systems and atmospheric blocking (Broccoli and Manabe 1987; Roe and Lindzen 2001; Löfverström et al. 2014; Ding et al. 2024). These circulation changes displace the Atlantic Jet Stream southward and redirect storm tracks, particularly during winter, with profound consequences for European climate (Pausata et al. 2011; Hofer et al. 2012).

In the simulations analysed here, LGM exhibits significantly lower mean annual near-surface air temperatures over Europe, including regions over the ice sheets, with anomalies ranging from −7.6 to −11.8 °C relative to PI conditions, and global mean cooling of 3.7 to 6.8 °C. This pronounced cooling is primarily driven by the high albedo and elevation of the ice sheets (Kageyama et al. 2021), but is further reinforced by the strong katabatic winds and the restricted northward extension of warmer North Atlantic SSTs. Katabatic winds are particularly prominent along the margins of the Fennoscandian Ice Sheet, where extremely cold air masses flow downslope into adjacent forelands. Evidence from loess sequences in south-eastern Poland and Ukraine indicates abrupt and persistent north-to-south katabatic wind activity around 22.7 ka, coinciding with the maximum ice-sheet extent (Nawrocki et al. 2019, 2025).

The southward expansion of cold air masses leads to markedly reduced winter temperatures across central Europe and contributes to a strong meridional temperature gradient from the ice-sheet margins toward the Mediterranean, a feature that is more pronounced in winter than in summer. While PMIP4 general circulation models reproduce the large-scale pattern of cold-air outflow from major ice sheets (Conroy et al. 2019; Nawrocki et al. 2019), they tend to underestimate the local intensity and abruptness of katabatic winds inferred from high-resolution proxy records, highlighting the potential importance of regional climate modelling and downscaling approaches (Barthélemy et al. 2012; Heinemann 2020).

During summer, wind anomalies become zonal over central Europe. This leads to confined cooling close to the ice sheets. A dominant westerly aspect of wind systems during the LGM is also seen in proxy reconstructions, inferred from research on wind-blown (aeolian) sediments (Renssen et al. 2007). However, this notion has been contested recently in favour of prevailing easterly wind directions during that time (Schaffernicht et al. 2020).

Consistent with the colder thermal state, annual mean North Atlantic SSTs during the LGM are approximately 1.35 °C lower than in PI and LIG127k simulations, while sea-level pressure over the North Atlantic–European sector is higher by around 15 hPa. These conditions decrease the moisture transport towards Europe, resulting in a multi-model mean decrease in annual precipitation of approximately 20%. However, the mean distribution over all models is skewed by the much drier state of INM-CM4-8. Precipitation reductions are strongest over central Europe, whereas southern regions, particularly the Iberian Peninsula, experience slightly wetter conditions relative to PI. This localised increase in precipitation is linked to a marked southward shift in the surface zonal winds and in the intensity and position of the Icelandic Low. This is facilitated by a more equatorward storm track and enhanced cyclonic activity over the western Mediterranean despite overall colder conditions (Harrison et al. 1992; Ludwig et al. 2016). The finding of relatively humid conditions in Iberia during LGM is also expressed in palaeoecological proxy data (Naughton et al. 2007; Gomes et al. 2025) and the absence of LGM loess from the region (Wolf et al. 2021).

Across much of Europe, however, the prevalence of a glacial anticyclone also helped establish a cold, dry, and stable climate (Harrison et al. 1992; Ludwig et al. 2017), consistent with evidence from loess–palaeosol sequences indicating peak aridity and wind intensity in central Europe during the LGM (Antoine et al. 2009).

Taken together, the strong ice-sheet forcing, altered jet position, enhanced blocking, and reduced moisture availability characteristics of the mean state establish a fundamentally different dynamical background for atmospheric variability over the North Atlantic during the LGM. Such conditions are expected to influence both the structure and surface impact of dominant modes of variability, including the NAO. These shifts are analysed in the context of the LGM and LIG127k periods in the subsequent sections.

The LIG127k represents a warm climate state driven primarily by orbital forcing, with higher global and European mean temperatures relative to the PI period. In the simulations analysed here, European temperatures exceed PI levels on an annual mean basis, but the dominant feature of the LIG127k climate is an enhanced seasonal contrast rather than a uniform warming. Summers are substantially warmer (2.7–4 °C), while winters (0.2–1.65 °C) are slightly cooler over much of Europe than PI. This amplified seasonality is consistent with increased orbital obliquity during the LIG127, in conjunction with enhanced summer insolation at high northern latitudes and reduced winter insolation. This specific insolation pattern is, however, only representative of the applied 127 ka time slice and was reversed toward the end of the LIG127k. Specifically, for the European sector, the LIG127k orbital configuration resulted in a significant increase in summer solar forcing, with June insolation anomalies exceeding 60–70 W m^{-2} across northern Europe (see Fig. 1 in Otto-Bliesner et al. 2021). Strongly decreased seasonality throughout much of the remaining interglacial is, e.g., evidenced by the wider distribution of non-frost-resistant plant species than today (Zagwijn 1996; Velichko et al. 2005).

Summer warming is strongest over eastern and central Europe, whereas regions closer to the North Atlantic experience a weaker temperature response, reflecting the moderating influence of the ocean. The land-sea contrast varies considerably across models. Further, the northward distribution of the warmer SST during the LIG127k, in combination with a more zonal circulation pattern, leads to warmer and wetter conditions in northern Europe, while southern Europe experienced drying, particularly during summer. These results represent a mismatch with findings from continental pollen records. Unlike today, during the LIG127k, there was a latitudinally uniform vegetation pattern from Central Europe to the east, indicating a less pronounced continentality gradient along this section (Turner 2000; Gibbard and Knudsen 2025). This effect was facilitated by higher eustatic sea levels during the LIG127k (Dutton and Lambeck 2012), forming a direct marine connection from both the North and Baltic Seas to the White Sea and thus providing an extension of more oceanic climates in Eastern Europe (Miettinen et al. 2014). However, because the PMIP simulations assume modern land-sea distributions, regional biases may exist in areas sensitive to palaeo-coastline changes.

4.2 Atmospheric variability across different time periods

The leading modes of North Atlantic atmospheric variability remain similar across periods and models, indicating that the fundamental patterns of large-scale variability persist across different climate states, despite a few substantial differences. In particular, the NAO consistently emerges as the dominant mode of wintertime sea-level pressure variability, followed by the EA pattern. NAO and EA together account for more than half of the total SLP variance, with the largest combined contribution during the LGM. The clear separation in explained variance between the leading modes, particularly during the LGM, indicates more established variability patterns, whereas reduced separation during warmer periods reflects a more heterogeneous variability pattern. However, while the spatial structure of these modes is broadly preserved, their amplitude, variance explained, and spatial positioning exhibit systematic state dependence, highlighting the sensitivity of atmospheric variability to mean climate conditions. Particularly, the NAO dipole structure is consistent across periods and models. The NAO has a stronger and more spatially confined dipole structure, with enhanced pressure gradients between the subpolar and subtropical North Atlantic during the LGM, while the dipole is weaker during the LIG127k.

The southward and longitudinal displacement of NAO pressure centres during the LGM is in agreement with previous modelling studies, indicating ice-sheet-driven shifts in circulation regimes. Although the displacement can be seen in the CMIP5 models' PI simulations compared to observations (Wang et al. 2017), the displacement here is relative to PI, along with the independence of AMO phases (in contrast to Börgel et al. 2020) among the periods. This further reinforces the state dependence of these shifts, and it also supports the findings of the LGM simulation of Justino and Peltier (2005). In contrast, the PI and LIG127k exhibit more similar expressions of NAO variability, both in terms of spatial structure and variance distribution. The higher pattern correlations between these two interglacial states indicate that, despite differences in orbital forcing and seasonal insolation (see Fig. 1 in Otto-Bliesner et al. 2021), the large-scale dynamical controls on North Atlantic variability remain similar. The weaker NAO dipole during the LIG127k is particularly associated with a reduced subtropical high-pressure anomaly.

Seasonal contrasts further emphasise this state dependence. While winter variability is dominated by canonical large-scale modes, summer variability exhibits reduced variance, weaker mode separation, and greater structural heterogeneity across models, complicating the physical interpretation of individual modes. During the LGM, the loss of NAO dominance in summer and the emergence of alternative patterns suggest a seasonal weakening of the dynamical constraints that organise wintertime circulation. During the summer, in the present and historical climate, SCA is commonly represented as the second mode following the NAO, with EA as the third mode (Hall and Hanna 2018). This pattern is seen during warm periods. However, SCA is absent in the first two modes of the LGM. In interglacial climates, summer variability more closely resembles the observed summer NAO structure, albeit with substantially lower variance, highlighting the weaker and less organised summertime circulation variability.

The consistent instantaneous relationship between the NAO and the NAT across all periods indicates that large-scale atmospheric forcing remains the primary driver of SST variability on interannual timescales, irrespective of the background climate. The absence of a robust and consistent lagged low-frequency relationship between the NAO and the AMO across models, even in the PI simulations, indicates the models' lack of capturing either the low-frequency part of the NAO variability or the AMO or both, particularly given the limited temporal extent of the simulations analysed.

The persistence of a basin-scale tripole pattern in net downward surface heat flux associated with NAO variability across all the periods demonstrates a robust modulation of air–sea energy exchange by atmospheric circulation. This relation is strongest and most spatially coherent during the LGM, consistent with enhanced heat flux gradients and reduced ocean stratification under colder conditions. Similarly, the NAO-related dipole in mixed layer depth reflects a dynamically coherent ocean response, linking atmospheric forcing to the subsurface ocean.

The NAO remains the dominant mode of wintertime atmospheric variability across the periods, but its influence on surface temperature is weaker during the LGM. This suggests that glacial boundary conditions, such as ice sheet topography and increasing atmospheric stability, could inhibit the efficient surface coupling of NAO-related pressure anomalies. Interestingly, models such as INM-CM4-8 and MPI-ESM1-2-LR during the LGM show a monopole warming pattern rather than the canonical dipole, likely due to a northwest–southeast alignment of the NAO pressure centres in these simulations. This reflects possible structural shifts in the NAO under glacial conditions. The second mode, corresponding to the EA pattern, shows a more zonally oriented influence, resulting in a pronounced cooling over southern and western Europe, especially over the Mediterranean. Its impact is often stronger than that of the NAO in these regions, particularly during the LIG127k. However, the strength and spatial coherence of the EA teleconnection vary widely across models. Precipitation responses display the characteristic NAO-related tripole structure, with drying over central Europe and enhanced precipitation over Scandinavia, although the magnitude intensifies during the LGM. The EA mode, by contrast, shows a continent-wide drying effect with limited regions of wet anomalies, suggesting its role in widespread winter drying.

4.3 Inter-model consistency and structural uncertainties

The comparison of models in our study reveals considerable differences in how these climatic features are simulated. The models show a range of 3.73–6.8 °C cooling in LGM and 0.11 °C to 0.4 °C cooling during the LIG127k, compared to the PI, in annual global mean near-surface air temperatures. The whole spectrum of CMIP6 models shows a 3.26 °C to 7.17 °C colder LGM (Kageyama et al. 2021), and the change of −0.48 °C to 0.56 °C for the LIG127k (Otto-Bliesner et al. 2021). While in proxy reconstructions, cooling is 4 to 6 °C during the LGM (Annan and Hargreaves 2015), the LIG127k was 1.9 °C warmer (Turney and Jones 2010).

Even within the six models considered here, notable differences emerge. For instance, the MIROC-ES2L model consistently shows wetter conditions, especially during the LGM, and CESM2 simulates the warmest near-surface air temperatures, while INM-CM4-8 produces the coldest and driest conditions. It is important to note that the ranking of models by global Equilibrium Climate Sensitivity (ECS) does not always correspond to the magnitude of their regional response over Europe. For instance, while AWI-ESM-1-1-LR and CESM2 exhibit the highest ECS (3.6) and INM-CM4-8 the lowest (2.1) among the PMIP4 ensemble (Kageyama et al. 2021), INM-CM4-8 simulates the coldest LGM conditions over the European sector. This highlights that local feedbacks, such as the expansion of North Atlantic SST feedback or changes in the atmosphere and ocean circulation, can override global sensitivity patterns, leading to extreme regional cooling even in models with comparatively low global climate sensitivity. The amount of spread in monthly mean surface temperature between models is particularly pronounced during LGM winters, where models show a 40% greater spread (difference between the warmest and coldest models) compared to interglacial periods (Fig. 1).

The spread in SSTs is consistent throughout the year during the LGM, albeit with a larger spread during the LIG127k. SST cooling is highest in CESM2 and MIROC-ES2L. While CESM2-WACCM-FV2 shows the maximum sea ice extent, MPI-ESM1-2-LR and AWI-ESM-1-1-LR show the lowest sea ice extent. This might have been caused by the northward extension of warm SSTs in AWI-ESM-1-1-LR and MPI-ESM1-2-LR. For the climatology, AWI-ESM-1-1-LR and MPI-ESM1-2-LR are more similar, whereas CESM2 and CESM2-WACCM-FV2 show a higher degree of similarity in their variability patterns. The observed similarities in climatology between AWI-ESM-1-1-LR and MPI-ESM1-2-LR, despite their distinct institutional origins, can to some extent be explained by the use of the same underlying atmospheric model component. The similarity in the variability patterns between CESM2 and CESM2-WACCM-FV2 (both part of the Community Earth System Model (CESM) family, with CESM2-WACCM-FV2 incorporating a more comprehensive representation of the middle and upper atmosphere) can also be explained by their shared foundational modelling framework. However, simulations with different initial conditions, parameter settings and/or underlying ice sheet configurations indicated that the same model can simulate a different climate response and climate variability during the LGM (Kapsch et al. 2022; Mikolajewicz et al. 2025). During LGM, AWI-ESM-1-1-LR's SLP is ~ 15 hpa higher compared to other models. Here, the difference in Azores High (LGM-PI) is 2–3 times larger than in other models. For MIROC-ES2L, the Icelandic Low is shifted more than 5° south during LGM and 10° during PI compared to other models.

4.4 Limitations and future directions

This study demonstrates that European climate variability is a robust pattern and also highlights certain changes under different background climate states, with substantial inter-model spread emerging under extreme conditions such as the LGM and LIG127k. While agreement is relatively high for PI, the larger discrepancies during past climates do not necessarily reflect poor model performance, but rather expose structural uncertainties in representing processes that are weak or absent in the modern climate, including ice-sheet-driven circulation changes, katabatic winds, and altered ocean dynamics.

Moreover, recent studies (e.g., Kapsch et al. 2022; Mikolajewicz et al. 2025) emphasise that incorporating interactive ice sheets and associated feedbacks is crucial for realistically simulating long-term climate variability. Although these processes are suppressed in the quasi-equilibrium framework adopted here, this limitation highlights that the advances in Earth system feedback representation are as important as increasing spatial resolution, particularly for simulations of different palaeoclimate states.

5 Conclusion

The Last Glacial Maximum (LGM) and the Last Interglacial (LIG127k) represent climate states governed by fundamentally different climate forcing, offering valuable insights into the climate dynamics and serving as test beds for evaluating climate models. This study investigates changes in circulation patterns and climate variability over the North Atlantic and Europe during the LGM and LIG127k, using six CMIP6/PMIP4 climate model simulations.

Compared to PI, LGM is characterised by lower summer insolation, extensive ice sheets, and cooler sea surface temperatures (SSTs), which led to substantial cooling and reduced precipitation over Europe through pronounced changes in atmospheric circulation. The Icelandic Low shifted southward, and the North Atlantic exhibited a substantially higher sea level pressure (SLP) with changes in spatial pattern. The strong surface winds originating from the ice sheets reinforced conditions over Europe (particularly during winter), and the altered winds from the Atlantic influenced regional precipitation.

The LIG127k simulations show near PI global mean temperatures with enhanced seasonality over Europe by summer warming (2.7–4 °C) and slight winter cooling (0.2–1.65 °C). Northern Europe experienced warmer and wetter conditions, likely due to northward-shifted SST and zonal circulation along with changes in orbital forcing, while southern Europe faced drying, particularly in summer.

The leading modes of North Atlantic atmospheric winter variability remain identifiable across all climate states considered, indicating that the fundamental patterns of variability are robust even across glacial and interglacial conditions. The NAO consistently dominates wintertime sea-level pressure variability during the LGM, LIG127k, and PI, while its spatial structure, amount of variance, and seasonal persistence exhibit clear state dependence. In particular, the LGM is characterised by a stronger and more spatially confined NAO dipole and enhanced winter variance, whereas the LIG127k displays a weaker dipole structure. Summer variability is substantially weaker and less organised, especially during the LGM, highlighting a reduced dynamical constraint on atmospheric circulation under glacial conditions.

The coupling between atmospheric variability and the ocean remains a persistent feature across all periods. The robust instantaneous relationship between the NAO and the North Atlantic SST tripole demonstrates that atmospheric forcing consistently drives the interannual SST variability, independent of background climate. In contrast, no stable low-frequency coupling with the AMO emerges, reflecting both model uncertainty and the limited temporal extent of equilibrium simulations. NAO-related anomalies in surface heat fluxes and mixed layer depth further reveal a dynamically coherent oceanic response, which is strongest during the LGM, consistent with enhanced air–sea coupling under colder and less stratified conditions.

Overall, these results demonstrate that while the dominant modes of North Atlantic variability are structurally robust across extreme climate states, their expression, seasonal dominance, and oceanic imprint are strongly modulated by mean climate conditions. This state dependence has important implications for interpreting past climate variability and for assessing the applicability of present-day circulation patterns to fundamentally different climatic regimes.

Model comparisons reveal considerable inter-model differences in simulating LGM and LIG127k climatic features compared to PI. These discrepancies, particularly during the LGM, do not necessarily imply poor model performance but rather reflect uncertainties associated with simulating climate states that differ strongly from present-day conditions. In particular, differences in the representation of ice sheets, atmospheric circulation, sea ice, and related feedbacks contribute to the spread among models.

These findings underscore the importance of multi-model intercomparisons in palaeoclimate research and highlight the need for improved representation of key processes under extreme climate conditions. Beyond model intercomparison, climate models provide a complementary framework to proxy-based reconstructions by enabling process-based interpretations of past climate variability and its drivers.

Supplementary Information The online version contains supplementary material available at https://doi.org/10.1007/s00382-026-08278-x.

Acknowledgements This research was financed by the Lower Saxony MWK with funds from the *zukunft.niedersachsen* program of the VolkswagenStiftung, as part of the project *Climate Change and Early Humans in the North (CCEHN)*. MLK received funding from the German Federal Ministry of Research, Technology and Space as a Research for Sustainability Initiative through the PalMod project (Grant No. 01LP2302A). We thank Prof. Dr. Thomas Terberger and Tilman Böckenförde for their valuable support in editing the manuscript. We also acknowledge the CMIP6 modelling community for providing the simulation data used in this study.

Author contributions All authors contributed to the study conception and design. Material preparation, data collection, and analysis were performed by Deepak Kumar, Sebastian Wagner, and Antje Schwalb. Deepak Kumar wrote the first draft of the manuscript, and all authors commented on previous versions of the manuscript. Sebastian Wagner, Michael Hein, Antje Schwalb, and Marie-Luise Kapsch provided critical feedback that helped refine the discussion and improve the manuscript. All authors read and approved the final manuscript.

Funding Open Access funding enabled and organized by Projekt DEAL. This research was financed by the Lower Saxony MWK with funds from the zukunft.niedersachsen program of the VolkswagenStiftung, Grants No. ZN3985, as part of the project Climate Change and Early Humans in the North (CCEHN).

Data availability All model data used in this study were retrieved from the CMIP6 archive via the Earth System Grid Federation (ESGF) data portals. The specific experiments used include *piControl* (preindustrial control), *lig127k* (Last Interglacial), and *lgm* (Last Glacial Maximum). These datasets are publicly available and can be accessed through https://esgf-metagrid.cloud.dkrz.de/search/cmip6/.

Declarations

Competing interests The authors have no relevant financial or non-financial interests to disclose.

References

AndréL B (1978) Long-term variations of daily insolation and quaternary climatic changes. J Atmos Sci 35:2362–2367. https://doi.org/10.1175/1520-0469(1978)035%3c2362:LTVODI%3e2.0.CO;2

Annan JD, Hargreaves JC (2013) A new global reconstruction of temperature changes at the Last Glacial Maximum. Climate Past 9:367–376. https://doi.org/10.5194/cp-9-367-2013

Annan JD, Hargreaves JC (2015) A perspective on model-data surface temperature comparison at the Last Glacial Maximum. Quatern Sci Rev 107:1–10. https://doi.org/10.1016/j.quascirev.2014.09.019

Annan JD, Hargreaves JC, Mauritsen T (2022) A new global surface temperature reconstruction for the Last Glacial Maximum. Clim Past 18:1883–1896. https://doi.org/10.5194/cp-18-1883-2022

Antoine P, Rousseau D-D, Moine O et al (2009) Rapid and cyclic aeolian deposition during the Last Glacial in European loess: a high-resolution record from Nussloch, Germany. Quatern Sci Rev 28:2955–2973. https://doi.org/10.1016/j.quascirev.2009.08.001

Årthun M, Kolstad EW, Eldevik T, Keenlyside NS (2018) Time scales and sources of European temperature variability. Geophys Res Lett 45:3597–3604. https://doi.org/10.1002/2018GL077401

Barnston AG, Livezey RE (1987) Classification, seasonality and persistence of low-frequency atmospheric circulation patterns. Mon Wea Rev 115:1083–1126. https://doi.org/10.1175/1520-0493(1987)115%3c1083:CSAPOL%3e2.0.CO;2

Barthélemy A, Goosse H, Mathiot P, Fichefet T (2012) Inclusion of a katabatic wind correction in a coarse-resolution global coupled climate model. Ocean Model 48:45–54. https://doi.org/10.1016/j.ocemod.2012.03.002

Beranová R, Huth R (2008) Time variations of the effects of circulation variability modes on European temperature and precipitation in winter. Int J Climatol 28:139–158. https://doi.org/10.1002/joc.1516

Börgel F, Frauen C, Neumann T, Markus Meier HE (2020) The Atlantic Multidecadal Oscillation controls the impact of the North Atlantic Oscillation on North European climate. Environ Res Lett 15:104025. https://doi.org/10.1088/1748-9326/aba925

Broccoli AJ, Manabe S (1987) The influence of continental ice, atmospheric CO2, and land albedo on the climate of the last glacial maximum. Clim Dyn 1:87–99. https://doi.org/10.1007/BF01054478

Burke KD, Williams JW, Chandler MA et al (2018) Pliocene and Eocene provide best analogs for near-future climates. Proc Natl Acad Sci USA 115:13288–13293. https://doi.org/10.1073/pnas.1809600115

CAPE-Last Interglacial Project (CLIP) Members (2006) Last Interglacial Arctic warmth confirms polar amplification of climate change. Quatern Sci Rev 25:1383–1400. https://doi.org/10.1016/j.quascirev.2006.01.033

Cariou E, Cattiaux J, Qasmi S et al (2025) Linking European temperature variations to atmospheric circulation with a neural network: a pilot study in a climate model. Geophys Res Lett 52:e2024GL113540. https://doi.org/10.1029/2024GL113540

Cleator SF, Harrison SP, Nichols NK et al (2020) A new multivariable benchmark for Last Glacial Maximum climate simulations. Clim Past 16:699–712. https://doi.org/10.5194/cp-16-699-2020

Comas-Bru L, Hernández A (2018) Reconciling North Atlantic climate modes: revised monthly indices for the East Atlantic and the Scandinavian patterns beyond the 20th century. Earth Syst Sci Data 10:2329–2344. https://doi.org/10.5194/essd-10-2329-2018

Comas-Bru L, McDermott F (2014) Impacts of the EA and SCA patterns on the European twentieth century NAO–winter climate relationship. Quart J R Meteoro Soc 140:354–363. https://doi.org/10.1002/qj.2158

Conroy JL, Karamperidou C, Grimley DA, Guenthner WR (2019) Surface winds across eastern and midcontinental North America during the Last Glacial Maximum: a new data-model assessment. Quatern Sci Rev 220:14–29. https://doi.org/10.1016/j.quascirev.2019.07.003

Cropper T, Hanna E, Valente MA, Jónsson T (2015) A daily Azores-Iceland North Atlantic Oscillation index back to 1850. Geoscience Data J 2:12–24. https://doi.org/10.1002/gdj3.23

Danabasoglu G (2019a) NCAR CESM2 model output prepared for CMIP6 PMIP lig127k. Earth System Grid Federation. https://doi.org/10.22033/ESGF/CMIP6.7673

Danabasoglu G (2019b) NCAR CESM2-WACCM-FV2 model output prepared for CMIP6 CMIP piControl. Earth System Grid Federation. https://doi.org/10.22033/ESGF/CMIP6.11302

Danabasoglu G, Lawrence D, Lindsay K et al (2019) NCAR CESM2 model output prepared for CMIP6 CMIP piControl. Earth System Grid Federation. https://doi.org/10.22033/ESGF/CMIP6.7733

Danek C, Shi X, Stepanek C et al (2020) AWI AWI-ESM1.1LR model output prepared for CMIP6 CMIP piControl. Earth System Grid Federation. https://doi.org/10.22033/ESGF/CMIP6.9335

Davis BAS, Brewer S (2009) Orbital forcing and role of the latitudinal insolation/temperature gradient. Clim Dyn 32:143–165. https://doi.org/10.1007/s00382-008-0480-9

Ding H, Dong L, Liu K et al (2024) Impacts of Greenland ice sheet on blocking in idealized simulations. J Clim 37:4961–4987. https://doi.org/10.1175/JCLI-D-23-0229.1

Dutton A, Lambeck K (2012) Ice volume and sea level during the last interglacial. Science 337:216–219. https://doi.org/10.1126/science.1205749

Eyring V, Bony S, Meehl GA et al (2016) Overview of the coupled model intercomparison project phase 6 (CMIP6) experimental design and organization. Geosci Model Dev 9:1937–1958. https://doi.org/10.5194/gmd-9-1937-2016

Folland CK, Knight J, Linderholm HW et al (2009) The summer North Atlantic oscillation: past, present, and future. J Clim 22:1082–1103. https://doi.org/10.1175/2008JCLI2459.1

Gibbard PL, Knudsen KL (2025) Palaeoenvironmental evolution of the Baltic Sea basin during the Last Interglacial (Eemian, Mikulino stages): a review. Boreas bor.70040. https://doi.org/10.1111/bor.70040

Gomes SD, Fletcher W, Stone A et al (2025) Rising atmospheric CO_2 concentrations: the overlooked factor promoting SW Iberian forest development across the LGM and the last deglaciation? Biogeosciences 22:6631–6650. https://doi.org/10.5194/bg-22-6631-2025

Hajima T, Abe M, Arakawa O et al (2019) MIROC MIROC-ES2L model output prepared for CMIP6 CMIP piControl. Earth System Grid Federation. https://doi.org/10.22033/ESGF/CMIP6.5710

Hall RJ, Hanna E (2018) North Atlantic circulation indices: links with summer and winter UK temperature and precipitation and implications for seasonal forecasting. Int J Climatol 38:5398. https://doi.org/10.1002/joc.5398

Harrison SP, Prentice IC, Bartlein PJ (1992) Influence of insolation and glaciation on atmospheric circulation in the North Atlantic sector: implications of general circulation model experiments for the Late Quaternary climatology of Europe. Quatern Sci Rev 11:283–299. https://doi.org/10.1016/0277-3791(92)90002-P

Heinemann G (2020) Assessment of regional climate model simulations of the katabatic boundary layer structure over Greenland. Atmosphere 11:571. https://doi.org/10.3390/atmos11060571

Hofer D, Raible CC, Dehnert A, Kuhlemann J (2012) The impact of different glacial boundary conditions on atmospheric dynamics and precipitation in the North Atlantic region. Clim Past 8:935–949. https://doi.org/10.5194/cp-8-935-2012

Hoffman JS, Clark PU, Parnell AC, He F (2017) Regional and global sea-surface temperatures during the last interglaciation. Science 355:276–279. https://doi.org/10.1126/science.aai8464

Hurrell JW (1995) Decadal Trends in the North Atlantic Oscillation: regional temperatures and precipitation. Science 269:676–679. https://doi.org/10.1126/science.269.5224.676

Hurrell JW, Deser C (2009) North Atlantic climate variability: the role of the North Atlantic Oscillation. J Mar Syst 78:28–41. https://doi.org/10.1016/j.jmarsys.2008.11.026

Izumi K, Bartlein PJ, Harrison SP (2013) Consistent large-scale temperature responses in warm and cold climates. Geophys Res Lett 40:1817–1823. https://doi.org/10.1002/grl.50350

Jing Y, Li Y, Xu Y (2020) Assessment of responses of North Atlantic winter sea surface temperature to the North Atlantic Oscillation on an interannual scale in 13 CMIP5 models. Ocean Sci 16:1509–1527. https://doi.org/10.5194/os-16-1509-2020

Jones PD, Jonsson T, Wheeler D (1997) Extension to the North Atlantic oscillation using early instrumental pressure observations from Gibraltar and south-west Iceland. Int J Climatol 17:1433–1450. https://doi.org/10.1002/(SICI)1097-0088(19971115)17:13%3c1433::AID-JOC203%3e3.0.CO;2-P

Jungclaus J, Mikolajewicz U, Kapsch M-L et al (2019) MPI-M MPI-ESM1.2-LR model output prepared for CMIP6 PMIP lgm. Earth System Grid Federation. https://doi.org/10.22033/ESGF/CMIP6.6642

Justino F, Peltier WR (2005) The glacial North Atlantic Oscillation. Geophys Res Lett 32:2005GL023822. https://doi.org/10.1029/2005GL023822

Kageyama M, Albani S, Braconnot P et al (2017) The PMIP4 contribution to CMIP6 – Part 4: scientific objectives and experimental design of the PMIP4-CMIP6 Last Glacial Maximum experiments and PMIP4 sensitivity experiments. Geosci Model Dev 10:4035–4055. https://doi.org/10.5194/gmd-10-4035-2017

Kageyama M, Braconnot P, Harrison SP et al (2018) The PMIP4 contribution to CMIP6 – Part 1: Overview and over-arching analysis plan. Geosci Model Dev 11:1033–1057. https://doi.org/10.5194/gmd-11-1033-2018

Kageyama M, Harrison SP, Kapsch M-L et al (2021) The PMIP4 Last Glacial Maximum experiments: preliminary results and comparison with the PMIP3 simulations. Clim Past 17:1065–1089. https://doi.org/10.5194/cp-17-1065-2021

Kapsch M, Mikolajewicz U, Ziemen F, Schannwell C (2022) Ocean response in transient simulations of the last deglaciation dominated by underlying ice-sheet reconstruction and method of meltwater distribution. Geophys Res Lett 49:e2021GL096767. https://doi.org/10.1029/2021GL096767

Lang N, Wolff EW (2011) Interglacial and glacial variability from the last 800 ka in marine, ice and terrestrial archives. Clim Past 7:361–380. https://doi.org/10.5194/cp-7-361-2011

Li J, Sun C, Jin F (2013) NAO implicated as a predictor of Northern Hemisphere mean temperature multidecadal variability. Geophys Res Lett 40:5497–5502. https://doi.org/10.1002/2013GL057877

Löfverström M, Caballero R, Nilsson J, Kleman J (2014) Evolution of the large-scale atmospheric circulation in response to changing ice sheets over the last glacial cycle. Clim Past 10:1453–1471. https://doi.org/10.5194/cp-10-1453-2014

Ludwig P, Schaffernicht EJ, Shao Y, Pinto JG (2016) Regional atmospheric circulation over Europe during the Last Glacial Maximum and its links to precipitation. JGR Atmos 121:2130–2145. https://doi.org/10.1002/2015JD024444

Ludwig P, Pinto JG, Raible CC, Shao Y (2017) Impacts of surface boundary conditions on regional climate model simulations of European climate during the Last Glacial Maximum. Geophys Res Lett 44:5086–5095. https://doi.org/10.1002/2017GL073622

Martin-Garcia GM (2019) Oceanic impact on european climate changes during the quaternary. Geosciences 9:119. https://doi.org/10.3390/geosciences9030119

McKay NP, Overpeck JT, Otto-Bliesner BL (2011) The role of ocean thermal expansion in Last Interglacial sea level rise: thermal expansion in LIG sea level rise. Geophys Res Lett 38:n/a-n/a. https://doi.org/10.1029/2011GL048280

Miettinen A, Head MJ, Knudsen KL (2014) Eemian sea-level highstand in the eastern Baltic Sea linked to long-duration White Sea connection. Quatern Sci Rev 86:158–174. https://doi.org/10.1016/j.quascirev.2013.12.009

Mikolajewicz U, Kapsch M-L, Schannwell C et al (2025) Deglaciation and abrupt events in a coupled comprehensive atmosphere–ocean–ice-sheet–solid-earth model. Clim past 21:719–751. https://doi.org/10.5194/cp-21-719-2025

Naughton F, Sanchez Goñi MF, Desprat S et al (2007) Present-day and past (last 25000 years) marine pollen signal off western Iberia. Mar Micropaleontol 62:91–114. https://doi.org/10.1016/j.marmicro.2006.07.006

Nawrocki J, Bogucki AB, Gozhik P et al (2019) Fluctuations of the Fennoscandian Ice Sheet recorded in the anisotropy of magnetic susceptibility of periglacial loess from Ukraine. Boreas 48:940–952. https://doi.org/10.1111/bor.12400

Nawrocki J, Mroczek P, Łanczont M, Standzikowski K (2025) Sudden appearance of katabatic wind in Central-Eastern Europe driven by Scandinavian Ice Sheet dynamics as recorded in Polish loess. Global Planet Change 246:104709. https://doi.org/10.1016/j.gloplacha.2025.104709

North Greenland Ice Core Project members (2004) High-resolution record of Northern Hemisphere climate extending into the last interglacial period. Nature 431:147–151. https://doi.org/10.1038/nature02805

O'ishi R, Abe-Ouchi A, Ohgaito R et al (2019) MIROC MIROC-ES2L model output prepared for CMIP6 PMIP lig127k. Earth System Grid Federation. https://doi.org/10.22033/ESGF/CMIP6.5645

Ohgaito R, Abe-Ouchi A, Abe M et al (2019) MIROC MIROC-ES2L model output prepared for CMIP6 PMIP lgm. Earth System Grid Federation. https://doi.org/10.22033/ESGF/CMIP6.5644

Otto-Bliesner BL, Marshall SJ, Overpeck JT et al (2006) Simulating Arctic climate warmth and icefield retreat in the last interglaciation. Science 311:1751–1753. https://doi.org/10.1126/science.1120808

Otto-Bliesner BL, Braconnot P, Harrison SP et al (2017) The PMIP4 contribution to CMIP6 – Part 2: two interglacials, scientific objective and experimental design for Holocene and Last Interglacial simulations. Geosci Model Dev 10:3979–4003. https://doi.org/10.5194/gmd-10-3979-2017

Otto-Bliesner BL, Brady EC, Zhao A et al (2021) Large-scale features of Last Interglacial climate: results from evaluating the *lig127k* simulations for the Coupled Model Intercomparison Project (CMIP6)–Paleoclimate Modeling Intercomparison Project (PMIP4). Climate Past 17:63–94. https://doi.org/10.5194/cp-17-63-2021

Overpeck JT, Otto-Bliesner BL, Miller GH et al (2006) Paleoclimatic evidence for future ice-sheet instability and rapid sea-level rise. Science 311:1747–1750. https://doi.org/10.1126/science.1115159

Pausata FSR, Li C, Wettstein JJ et al (2011) The key role of topography in altering North Atlantic atmospheric circulation during the last glacial period. Clim past 7:1089–1101. https://doi.org/10.5194/cp-7-1089-2011

Renssen H, Kasse C, Vandenberghe J, Lorenz SJ (2007) Weichselian late pleniglacial surface winds over northwest and central Europe: a model–data comparison. J Quat Sci 22:281–293. https://doi.org/10.1002/jqs.1038

Roe GH, Lindzen RS (2001) The mutual interaction between continental-scale ice sheets and atmospheric stationary waves. J Climate 14:1450–1465. https://doi.org/10.1175/1520-0442(2001)014%3c1450:TMIBCS%3e2.0.CO;2

Schaffernicht EJ, Ludwig P, Shao Y (2020) Linkage between dust cycle and loess of the Last Glacial Maximum in Europe. Atmos Chem Phys 20:4969–4986. https://doi.org/10.5194/acp-20-4969-2020

Shi X, Yang H, Danek C, Lohmann G (2020a) AWI AWI-ESM1.1LR model output prepared for CMIP6 PMIP lgm. Earth System Grid Federation. https://doi.org/10.22033/ESGF/CMIP6.9330

Shi X, Yang H, Danek C, Lohmann G (2020b) AWI AWI-ESM1.1LR model output prepared for CMIP6 PMIP lig127k. Earth System Grid Federation. https://doi.org/10.22033/ESGF/CMIP6.9331

Spratt RM, Lisiecki LE (2016) A Late Pleistocene sea level stack. Clim past 12:1079–1092. https://doi.org/10.5194/cp-12-1079-2016

Sun C, Li J, Jin F-F (2015) A delayed oscillator model for the quasi-periodic multidecadal variability of the NAO. Clim Dyn 45:2083–2099. https://doi.org/10.1007/s00382-014-2459-z

Sutton RT, Hodson DLR (2005) Atlantic Ocean forcing of North American and European Summer Climate. Science 309:115–118. https://doi.org/10.1126/science.1109496

Tierney JE, Zhu J, King J et al (2020) Glacial cooling and climate sensitivity revisited. Nature 584:569–573. https://doi.org/10.1038/s41586-020-2617-x

Trenberth KE, Shea DJ (2006) Atlantic hurricanes and natural variability in 2005. Geophys Res Lett 33:2006GL026894. https://doi.org/10.1029/2006GL026894

Turner C (2000) The Eemian interglacial in the North European plain and adjacent areas. Neth J Geosci 79:217–231. https://doi.org/10.1017/S0016774600023660

Turney CSM, Jones RT (2010) Does the Agulhas Current amplify global temperatures during super-interglacials? J Quaternary Sci 25:839–843. https://doi.org/10.1002/jqs.1423

Velichko AA, Novenko EY, Pisareva VV et al (2005) Vegetation and climate changes during the Eemian interglacial in Central and Eastern Europe: comparative analysis of pollen data. Boreas 34:207–219. https://doi.org/10.1111/j.1502-3885.2005.tb01016.x

Velichko AA, Borisova OK, Zelikson EM (2008) Paradoxes of the Last Interglacial climate: reconstruction of the northern Eurasia climate based on palaeofloristic data. Boreas 37:1–19. https://doi.org/10.1111/j.1502-3885.2007.00001.x

Volodin E, Mortikov E, Gritsun A et al (2019a) INM INM-CM4–8 model output prepared for CMIP6 CMIP piControl. Earth System Grid Federation. https://doi.org/10.22033/ESGF/CMIP6.5080

Volodin E, Mortikov E, Gritsun A et al (2019b) INM INM-CM4–8 model output prepared for CMIP6 PMIP lgm. Earth System Grid Federation. https://doi.org/10.22033/ESGF/CMIP6.5075

Volodin E, Mortikov E, Gritsun A et al (2019c) INM INM-CM4–8 model output prepared for CMIP6 PMIP lig127k. Earth System Grid Federation. https://doi.org/10.22033/ESGF/CMIP6.5076

Wang X, Li J, Sun C, Liu T (2017) NAO and its relationship with the Northern Hemisphere mean surface temperature in CMIP5 simulations. JGR Atmos 122:4202–4227. https://doi.org/10.1002/2016JD025979

Wieners K-H, Giorgetta M, Jungclaus J et al (2019) MPI-M MPI-ESM1.2-LR model output prepared for CMIP6 CMIP piControl. Earth System Grid Federation. https://doi.org/10.22033/ESGF/CMIP6.6675

Wilks DS (2006) Statistical methods in the atmospheric sciences, 2nd edn. Academic Press, Amsterdam

Wolf D, Kolb T, Ryborz K et al (2021) Evidence for strong relations between the upper Tagus loess formation (central Iberia) and the marine atmosphere off the Iberian margin during the last glacial period. Quat Res 101:84–113. https://doi.org/10.1017/qua.2020.119

Yin Q, Berger A (2015) Interglacial analogues of the Holocene and its natural near future. Quatern Sci Rev 120:28–46. https://doi.org/10.1016/j.quascirev.2015.04.008

Yokoyama Y, Lambeck K, De Deckker P et al (2001) Erratum: correction: timing of the Last Glacial Maximum from observed sea-level minima. Nature 412:99–99. https://doi.org/10.1038/35083629

Yu H, Cheng S, Huang J et al (2024) Seasonal phase change of the North Atlantic tripole sea surface temperature predicted by air-sea coupling. Npj Clim Atmos Sci 7:322. https://doi.org/10.1038/s41612-024-00882-0

Zagwijn W (1996) An analysis of Eemian climate in Western and Central Europe. Quatern Sci Rev 15:451–469. https://doi.org/10.1016/0277-3791(96)00011-X